



Non-isothermal multi-dimensional direct methanol fuel cell model with micro-porous layers mitigating water/methanol crossover

Seunghun Jung*

Electrochemical Engine Center, Department of Mechanical and Nuclear Engineering, The Pennsylvania State University, University Park, PA 16802, USA

HIGHLIGHTS

- Non-isothermal multi-D DMFC with micro-porous layers is developed.
- This paper presents four types of DMFC with anode/cathode MPLs.
- The model explains interfacial saturation jump, water/methanol crossover.
- The model explains the non-isothermal effect on heat and mass transfer in DMFCs.
- Large-scale simulation of 28 cm² cell is conducted.

ARTICLE INFO

Article history:

Received 7 October 2012

Received in revised form

9 December 2012

Accepted 12 December 2012

Available online 27 December 2012

Keywords:

Direct methanol fuel cell

Modeling

Micro-porous layer

Crossover

ABSTRACT

A two-phase three-dimensional direct methanol fuel cell (DMFC) model with the capability of saturation jump is developed in order to investigate the effect of micro-porous layers (MPL) on the water/methanol crossover in a DMFC. It is found that hydrophobic MPL on the cathode side helps cathode catalyst layer reserve water whereas hydrophobic MPL on the anode side blocks liquid flow to the cathode side, which effectively reduces water/methanol crossover. As the water transport in a DMFC occurs in two-phase, energy equation considering the heat-pipe effect with latent heat is solved together. Calculation result revealed thermal conductivity of gas diffusion layer has a strong influence on both temperature and water transport. Finally, a large-scale simulation of 28 cm² cell is conducted to examine current density and fuel concentration distribution.

© 2013 Elsevier B.V. All rights reserved.

1. Introduction

Inside a direct methanol fuel cell (DMFC) several transport phenomena related to electrochemical reactions occur simultaneously. Methanol oxidation reaction (MOR) occurs on the anode side whereas oxygen reduction reaction (ORR) occurs on the cathode side. Water participates in MOR as a reactant and it is produced as a byproduct from ORR in the cathode. Therefore, theoretically, it is possible to operate a DMFC without external supply of water [1]. Such situation is called as 'water neutral condition'. This is very desirable because user should carry only pure methanol without water, which significantly reduce the volume and weight of the DMFC system. In order to construct such an ideal

DMFC, it is important to know the fundamentals of transport phenomena which occur three-dimensionally in a DMFC. Many experimental studies about these transport phenomena in fuel cells have been conducted. However, there is a limitation of such experiments because it is difficult to visualize and measure the species transport inside porous media of a fuel cell, which three-dimensionally occurs in very small scale (thickness of typical porous media is around 0.3 mm). Multi-dimensional fuel cell model incorporated with computational fluid dynamics (CFD) is a powerful tool for the understanding the fundamentals of transport phenomena in a fuel cell.

Multi-dimensional DMFC model framework was established by Wang and Wang [2], and Liu and Wang [3]. Wang's model was two-dimensional and isothermal. Liu's model extended two-dimensional model to three-dimensional but it was still isothermal model. Capability of non-isothermal modeling is important for predicting non-uniform behavior such as evaporation/condensation of water and latent heat effect on heat removal in a fuel cell. In addition, both of previous models didn't consider the effect

* Present address: Battery R&D, LG Chem Research Park, 104-1 Moonji-dong, Yuseong-gu, Daejeon 305-380, Republic of Korea. Tel.: +82 10 8443 5214; fax: +82 42 862 1981.

E-mail addresses: stratus76@hotmail.com, stratus760@gmail.com.

of micro-porous layer which is proved to be very effective for minimizing water/methanol crossover by generating saturation jumps at the interface of porous media.

In this paper, firstly we introduce the two-phase non-isothermal multi-dimensional DMFC model, which is developed to identify and simulate the transport phenomena and to predict the cell performance and the fuel efficiency. Secondly, with the developed model, the effect of micro-porous layer on water/methanol crossover is simulated and visualized by applying saturation jump sub-model. Thirdly, non-isothermal behavior such as cathode side heat removal by the heat-pipe effect is simulated and discussed. Finally, a full-scale simulation of 28 cm² DMFC cell is introduced.

2. Physical model

The present multi-dimensional model is extended from the work by Wang and Wang [2], and Liu and Wang [3]. Important extended capabilities are saturation jump, non-isothermal behavior and large-scale simulation with parallel processing. Governing equations for the present multi-dimensional DMFC model are

summarized in Table 1, and constitutive relationships are listed in Table 2.

2.1. Mass transport in a typical DMFC

The structure of a single channel in a typical DMFC is presented in Fig. 1 which is created for the present multi-dimensional model. On the anode side, liquid fuel mixture is introduced from the inlet of the anode channel by a liquid pump. Introduced liquid fuel is transported to the anode GDL surface and spread throughout the anode porous media, then consumed in the anode catalyst layer by MOR. On the cathode side, oxidizer (typically air) is introduced from the inlet of the cathode channel by a blower. Introduced oxidizer is diffused throughout the cathode porous media and consumed in the cathode catalyst layer by ORR.

2.2. Description of mass transport on the anode GDL surface

Several studies [2,4,5] explain mass transfer at the anode channel/GDL interface by convective mass transfer which can be obtained by heat transfer analogy as follows:

$$\begin{aligned} \dot{m}_l'' &= h_{m,l}(c_{l,A} - c_{l,B}) = \frac{Sh_l D_l}{\delta} (c_{l,A} - c_{l,B}) \quad (\text{Z.H. Wang, 2003}) \\ \dot{m}_i'' &= h_{m,i}(\rho_i - \rho_{i,\infty}) = \frac{Sh_D D_{m,i}}{\delta} (\rho_i - \rho_{i,\infty}) \quad (\text{J.H. Nam, 2003}) \\ \dot{m}_{\text{H}_2\text{O}}'' &= h_m(c_A^{\text{H}_2\text{O}} - c_B^{\text{H}_2\text{O}}) = \frac{Sh_D D^{\text{H}_2\text{O}}}{\delta} (c_A^{\text{H}_2\text{O}} - c_B^{\text{H}_2\text{O}}) \quad (\text{U. Pasaogullari, 2004}) \\ \text{where } Sh &\begin{cases} = f(\text{Re}) \\ = 2.693 \text{ (Fully developed laminar flow)} \end{cases} \end{aligned} \quad (1)$$

Table 1
Governing equations of the baseline DMFC model.

	Conservation equations	Source terms
Mass	$\nabla \cdot (\rho \vec{u}) = S^m$	$S_{acl}^m = M^{\text{MeOH}} S^{\text{MeOH}} + M^{\text{H}_2\text{O}} S^{\text{H}_2\text{O}} + \frac{M^{\text{CO}_2} j}{6F}$ $S_{ccl}^m = M^{\text{H}_2\text{O}} S^{\text{H}_2\text{O}} + M^{\text{O}_2} S^{\text{O}_2} + \frac{M^{\text{CO}_2} j_{\text{xover}}}{6F}$
Momentum	$\nabla \cdot (\rho \vec{u} \vec{u}) = -\nabla p + \nabla \cdot \vec{\tau} + S^u$	$S^u = -\frac{\mu}{K} \vec{u}$ (in porous media domain)
Water transport	$\nabla \cdot (\rho \vec{u} Y^{\text{H}_2\text{O}}) = \nabla \cdot [\rho D_{\text{capill}} \nabla Y^{\text{H}_2\text{O}}] + S^{\text{H}_2\text{O}}$	$S_{acl}^{\text{H}_2\text{O}} = -\frac{j M^{\text{H}_2\text{O}}}{6F} - \frac{j M^{\text{H}_2\text{O}}}{F} \alpha$ $S_{ccl}^{\text{H}_2\text{O}} = \frac{j M^{\text{H}_2\text{O}}}{2F} + \frac{j_{\text{xover}} M^{\text{H}_2\text{O}}}{3F} + \frac{j M^{\text{H}_2\text{O}}}{F} \alpha$
Methanol transport	$\nabla \cdot (\rho \vec{u} Y^{\text{MeOH}}) = \nabla \cdot [\rho D_{\text{eff}}^{\text{MeOH}} \nabla Y^{\text{MeOH}}] + S^{\text{MeOH}}$	$S_{acl}^{\text{MeOH}} = -\frac{j}{6F} M^{\text{MeOH}} - \frac{j_{\text{xover}}}{6F} M^{\text{MeOH}}$
Oxygen transport	$\nabla \cdot (\rho \vec{u} Y^{\text{O}_2}) = \nabla \cdot [\rho D_{\text{g,eff}}^{\text{O}_2} \nabla Y^{\text{O}_2}] + \nabla \cdot [Y^{\text{O}_2} \vec{j}] + S^{\text{O}_2}$	$S_{ccl}^{\text{O}_2} = -\frac{j}{4F} M^{\text{O}_2} - \frac{j_{\text{xover}}}{4F} M^{\text{O}_2}$
Proton	$0 = \nabla \cdot (\kappa_{e,\text{eff}} \nabla \phi_e) + S_e^\phi$	$S_{e,acl}^\phi = j$ $S_{e,ccl}^\phi = -j_c + j_{\text{xover}}$
Electron	$0 = \nabla \cdot (\kappa_{s,\text{eff}} \nabla \phi_s) + S_s^\phi$	$S_{s,acl}^\phi = -j$ $S_{s,ccl}^\phi = j_c - j_{\text{xover}}$
Energy	$\nabla \cdot (\rho c_p \vec{u} T) = \nabla \cdot (\kappa_{\text{eff}} \nabla T) + S^T$ where $\begin{cases} \kappa_{\text{eff}} = k_{\text{gdl}} + h_{\text{fg}}^0 M^{\text{H}_2\text{O}} D_{\text{g,eff}}^{\text{H}_2\text{O}} \frac{dc_{\text{sat}}^{\text{H}_2\text{O}}}{dT} \\ S^T = S_{\text{sensible}}^T + S_{\text{latent}}^T \end{cases}$	$S_{\text{sensible},acl}^T = j \left(\eta + T \frac{dU^0}{dT} \right) + \frac{i^2}{\kappa_{\text{eff}}}$ $S_{\text{sensible},mem}^T = \frac{i^2}{\kappa_{\text{eff}}}$ $S_{\text{sensible},ccl}^T = j \left(\eta + T \frac{dU^0}{dT} \right) + \frac{i^2}{\kappa_{\text{eff}}} + j_{\text{xover}} \left(\eta + T \frac{dU^0}{dT} \right)$ $S_{\text{latent}}^T = \nabla \cdot (h_{\text{fg}}^0 \rho_l \vec{u}_l)$

Table 2

Constitutive relationships and parameters for the baseline DMFC model.

Parameters	Expression	Reference
Relative permeability	$k_{r,l} = s^n$; $k_{r,g} = (1-s)^n$	[15]
Methanol diffusivity (vapor)	$D_g^{\text{MeOH},\text{H}_2\text{O}} = D_g^{\text{MeOH},\text{CO}_2} = 1.96 \times 10^{-5} \left(\frac{T}{328.15} \right)^{1.823} \frac{1.013 \times 10^5 \text{ Pa}}{p} [\text{m}^2/\text{s}]$	[16]
Water diffusivity (vapor)	$D_g^{\text{H}_2\text{O},\text{CO}_2} = 2.01 \times 10^{-5} \left(\frac{T}{307} \right)^{1.823} \frac{1.013 \times 10^5 \text{ Pa}}{p} [\text{m}^2/\text{s}]$	[17]
Methanol diffusivity (liquid)	$D_l^{\text{MeOH},\text{H}_2\text{O}} = 1.4 \times 10^{-9} \left(\frac{647.3 - 298.15}{647.3 - T} \right)^6 [\text{m}^2/\text{s}]$	[18]
Oxygen diffusivity (gas)	$D_g^{\text{O}_2} = 3.57 \times 10^{-5} \left(\frac{T}{352} \right)^{1.823} \frac{101300.0}{p} [\text{m}^2/\text{s}]$	[17]
Water content in Nafion-membrane	$\lambda = \begin{cases} 22 & (s > 0.3) \\ 14 + 8s/0.3 & (s \leq 0.3) \\ 0.043 + 17.81RH - 39.85RH^2 + 36.0RH^3 & (\text{vapor}) \end{cases}$	[19,20]
Water diffusivity in Nafion-membrane	$D_{\text{mem}}^{\text{H}_2\text{O}} = 4.80 \times 10^{-11} \exp \left[2416 \left(\frac{1}{303} - \frac{1}{T} \right) \right] [\text{m}^2/\text{s}]$	Calibrated based on [19]
Methanol diffusivity in Nafion-membrane	$D_{\text{mem}}^{\text{MeOH}} = 1.5 \times 10^{-10} \exp \left[2416 \left(\frac{1}{303} - \frac{1}{T} \right) \right] [\text{m}^2/\text{s}]$	Calibrated based on [19]
Water EOD coefficient in Nafion-membrane	$n_d^{\text{H}_2\text{O}} = \begin{cases} \left[\frac{\lambda - 14}{8} \right] (n_{d,\text{ref}}^{\text{H}_2\text{O}} - 1) + 1 & (\text{for } \lambda \geq 14) \\ 1 & (\text{for } \lambda < 14) \end{cases}$	[21], [22]
Water reference EOD coefficient in Nafion	$n_{d,\text{ref}}^{\text{H}_2\text{O}} = 1.6767 + 0.0155(T - 273) + 8.9074 \times 10^{-5}(T - 273)^2$	[21]
Methanol drag coefficient in Nafion-membrane	$n_d^{\text{MeOH}} = n_d^{\text{H}_2\text{O}} \frac{c^{\text{MeOH}}}{c_{\text{tot}}}$	[3]
Ion conductivity of Nafion-membrane	$k_m = 0.1 \text{ (S/cm)} @ 60^\circ\text{C}$ (fully hydrated)	
Effective water vapor diffusivity	$D_{g,\text{eff}}^{\text{H}_2\text{O}} = D_g^{\text{H}_2\text{O}}(1-s)^n \varepsilon^n$	
J-Leverett function	$J(s) = \begin{cases} -1.263s^3 + 1.669s^2 - 0.966s + 0.56 & (\text{when } \theta_c < 90^\circ) \\ 1.263s^3 - 2.120s^2 + 1.417s & (\text{when } \theta_c > 90^\circ) \end{cases}$	

However, the basic assumption of this description is ‘permeable surface’. There is no information about hydrophobicity or permeability in this description. In other words, this expression works well when GDL surface has no hydrophobicity. However, many experimental results show good agreement with this description because actual GDL surface is not ideally hydrophobic or

hydrophilic since it is a mixture of carbon (hydrophilic) and PTFE (hydrophobic). If GDL surface is ideally hydrophobic (liquid impermeable), this description fails.

Another way to explain the mass transport is applying hydraulic pressure acting on the GDL surface. Displacing gas-phase by liquid-phase in hydrophobic porous media is called as drainage. There exist three methods to cause drainage: 1) gravitation, 2) centrifugal force, 3) externally applied liquid pressure. In a fuel cell, first and second methods are not applicable. In order to fill ideally hydrophobic porous media with liquid, we should apply high liquid pressure externally which is called ‘break-through pressure’, which is defined as follows:

$$p_b = \frac{4\sigma \cos \theta_c}{d} \quad (2)$$

Breakthrough pressure of GDL can be estimated,

$$p_{b,\text{gdl}} = \frac{4\sigma \cos \theta_{c,\text{gdl}}}{d_{\text{gdl}}} = \frac{4 \times 0.06 \times \cos 110^\circ}{10^{-5}} = 8.2 \text{ kPa} \quad (3)$$

This is pretty high value compared to the pressure applied in the anode channel of a conventional DMFC (few Pa). In addition, there exists CO_2 gas pressure in the anode. If external liquid pressure is applied to permeate the GDL surface, it should be at least,

$$p_l > p_b + p_g \quad (4)$$

But, actual mass transfer at the channel/GDL interface occurs without such a high external pressure. Therefore, surface liquid transport of a conventional DMFC can be explained by convective mass transfer description. If GDL surface is ideally hydrophobic (convective mass transfer fails) and channel is not pressurized enough (less than the breakthrough pressure of the GDL surface),

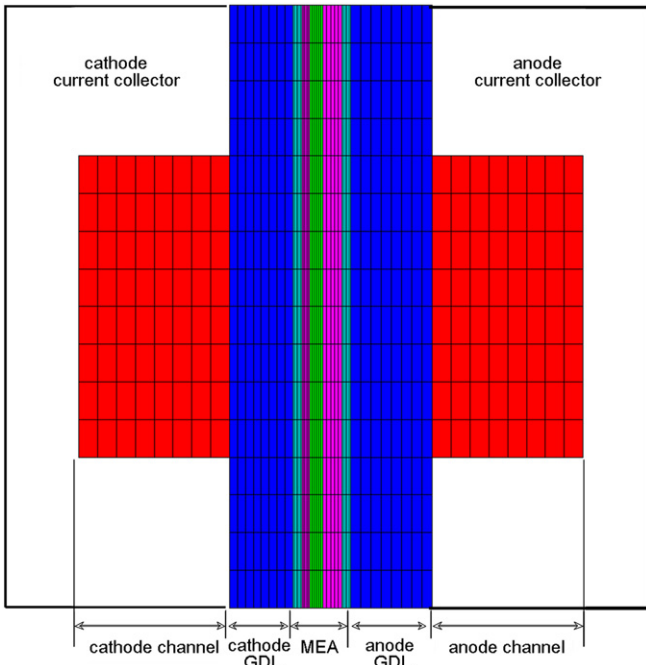


Fig. 1. Cross-sectional view of the DMFC for the present study.

then liquid transport is theoretically impossible and anode will not be wet.

On the cathode, as water is continuously produced by ORR, liquid water should be removed from the reaction site. Otherwise, liquid water will block the reaction site and ORR will be stopped. Liquid water removal from the cathode catalyst layer to the surface of the cathode channel can be easily explained by hydraulic pressure built by water production by ORR. As it is difficult for liquid water to permeate proton exchange membrane which has very low hydraulic permeability (or very high breakthrough pressure), liquid water produced in the cathode catalyst layer must move toward cathode GDL which has relatively lower breakthrough pressure. In addition, as the applied gas (air) pressure in the cathode is almost constant (\sim ambient pressure), liquid water can easily move through the hydrophobic GDL by drainage explained previously.

2.3. Description of mass transport in the anode porous media

It is difficult to explain liquid transport in the anode of a conventional DMFC with drainage theory because of following reasons. First, there is no or very low externally applied liquid pressure in the anode channel. Second, during liquid drainage in hydrophobic porous media, liquid-phase pressure must be greater than gas-phase pressure. However, in the anode of a conventional DMFC, gas-phase pressure (CO_2 pressure) must be greater than the liquid pressure in the channel. Otherwise, CO_2 gas cannot be removed out of the cell. Now we introduce phase-diffusion theory (M^2 model) developed by Wang and Cheng [6] in order to explain liquid transport in the anode of a DMFC here. M^2 model is appropriate for explaining multi-phase transport occurring in porous media, it is widely used for fuel cell modeling framework [2,3,5,10,14,21]. M^2 model considers the multi-phase system as a chemical mixture. Based upon this, M^2 model describes the multi-phase flow in terms of mass-averaged mixture flux velocity and phase-diffusive flux as follows:

$$\begin{aligned}\rho_l \vec{u}_l &= \vec{j}_l + \lambda_l \rho \vec{u} \\ \rho_g \vec{u}_g &= \vec{j}_g + \lambda_g \rho \vec{u}\end{aligned}\quad (5)$$

$$\text{where } \vec{j}_l = \frac{\lambda_l \lambda_g K}{\nu} \nabla p_c \text{ and } \vec{j}_l + \vec{j}_g = 0$$

Phase-diffusive flux (\vec{j}_l) is driven by the gradient of capillary pressure (p_c) defined as follows:

$$p_c = p_g - p_l = \sigma \cos \theta_c \left(\frac{\varepsilon}{K} \right) J(s) \quad (6)$$

Leverette's J -function (see Table 2) empirically expresses that capillary pressure is a function of liquid saturation defined as follows:

$$s = \frac{V_l}{V_{\text{pore}}} = 1 - \frac{V_g}{V_{\text{pore}}} = \frac{\rho_g Y^{\text{H}_2\text{O}} - \rho_g Y_g^{\text{H}_2\text{O}}}{\rho_l Y_l^{\text{H}_2\text{O}} - \rho_l Y^{\text{H}_2\text{O}} + \rho_g Y^{\text{H}_2\text{O}} - \rho_g Y_g^{\text{H}_2\text{O}}} \quad (7)$$

where two-phase mass fraction relationships are defined,

$$\rho Y^{\text{H}_2\text{O}} = \rho_l Y_l^{\text{H}_2\text{O}} s + \rho_g Y_g^{\text{H}_2\text{O}} (1 - s) \quad (8)$$

λ_l and λ_g express relative mobility of liquid and gas, respectively.

$$\lambda_l = \frac{k_{r,l} \nu}{k_{r,l} \nu_l + k_{r,g} \nu_g} \quad \text{and} \quad \lambda_g = 1 - \lambda_l \quad (9)$$

$$\text{where } \nu = \left(\frac{k_{r,l}}{\nu_l} + \frac{k_{r,g}}{\nu_g} \right)^{-1}$$

Relative permeabilities of each phase are expressed by semi-empirical Bruggeman relationship with liquid saturation as follows:

$$k_{r,l} = s^n \text{ and } k_{r,g} = (1 - s)^n \quad (10)$$

Phase-diffusion says that each phase moves in the opposite direction with the same mass flux. In order to drive this phase-diffusion, one of two-phases must become driving phase and the other phase becomes induced phase. In the anode, CO_2 gas is produced according to the reaction rate (electrical current). Therefore, gas pressure at A is higher than that of B and CO_2 gas flows from A to B in Fig. 2. As liquid-phase moves in the opposite direction of the gas flow by the definition of phase-diffusion of M^2 model, liquid phase induced from the anode channel moves from B to A.

$$\begin{aligned}\text{CH}_3\text{OH}(l) + \text{H}_2\text{O}(l) &\rightarrow \text{CO}_2(g) + 6\text{H}^+ + 6\text{e}^- \\ \dot{m}_l &= 32 + 18 = 50 \text{ g/s}(B \rightarrow A) \\ \dot{m}_g &= -48 \text{ g/s}(B \leftarrow A) \\ \dot{m}_{\text{net}} &= 50 - 48 = 2 \text{ g/s}(B \rightarrow A)\end{aligned}\quad (11)$$

When we consider above mass flux balance in the anode by assuming the net water transfer coefficient (α) is zero, we can see the amount of liquid flow and gas flow are similar and in the opposite direction. This supports the idea that phase-diffusion is the dominant mass transport mechanism in the porous media.

2.4. Two-phase water transport equation

As typical DMFCs operate under the water boiling point (100°C), water exists and moves in the form of two-phase (liquid water and water vapor) in a DMFC. In order to explain two-phase mass transfer, we adopt M^2 model [6] as the base of the present multi-dimensional model as follows:

$$\nabla \cdot (\rho \vec{u} Y^k) = \nabla \cdot [\rho_l D_{l,\text{eff}}^k \nabla Y_l^k + \rho_g D_{g,\text{eff}}^k \nabla Y_g^k] - \nabla \cdot [(Y_l^k - Y_g^k) \vec{j}_l] + S^k \quad (12)$$

Left term represents convective term which is significant in the flow channel region. First term on the right hand side represents the molecular diffusive term and second term is phase-

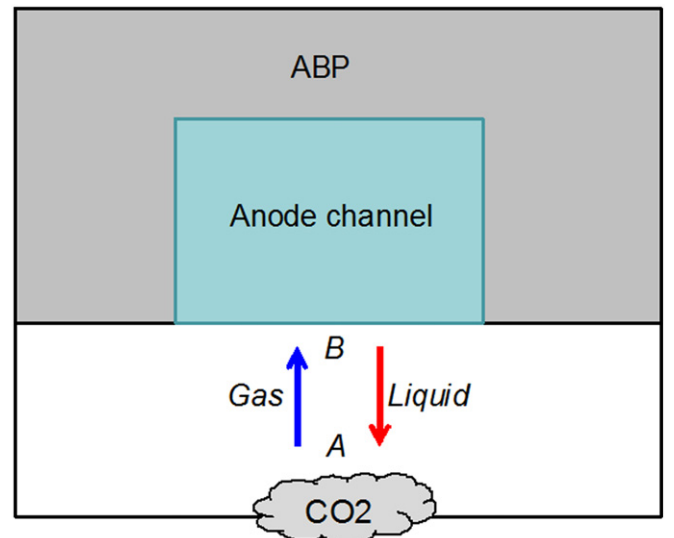


Fig. 2. Schematic of phase-diffusion in the anode.

diffusive term or capillary flux which is significant in the porous region. Capillary flux of liquid phase can be explained with Darcy's law as follows:

$$\vec{j}_l = \frac{\lambda_g \lambda_l K}{\nu} \nabla p_c \quad (13)$$

By plugging Eq. (6) into Eq. (13), capillary flux of liquid phase can be expressed as a function of liquid saturation as follows:

$$\begin{aligned} \vec{j}_l &= \frac{\lambda_g \lambda_l K}{\nu} \nabla p_c = \frac{\lambda_g \lambda_l K}{\nu} \nabla \left[\sigma \cos(\theta_c) \left(\frac{\epsilon}{K} \right)^{1/2} J(s) \right] \\ &= \frac{\lambda_g \lambda_l \sigma \cos(\theta_c) (K\epsilon)^{1/2}}{\nu} \frac{dJ}{ds} \nabla s \end{aligned} \quad (14)$$

By plugging Eq. (7) into Eq. (14), capillary diffusive flux can be reformed as follows:

$$\vec{j}_l = \frac{\lambda_g \lambda_l \sigma \cos(\theta_c) (K\epsilon)^{1/2}}{\nu} \frac{dJ}{ds} \frac{\rho_l (\rho_g Y_l^{\text{H}_2\text{O}} - \rho_g Y_g^{\text{H}_2\text{O}})}{(\rho_l Y_l^{\text{H}_2\text{O}} - \rho_l Y^{\text{H}_2\text{O}} + \rho_g Y^{\text{H}_2\text{O}} - \rho_g Y_g^{\text{H}_2\text{O}})^2} \nabla Y^{\text{H}_2\text{O}} \quad (15)$$

We can assume the water concentration in the gas phase is always saturated and the gradient of mass fraction in the liquid phase is almost zero due to dilute solution. Therefore, the water transport equation can be derived from Eq. (12) with Eq. (15) as follows:

$$\nabla \cdot (\rho \vec{u} Y^{\text{H}_2\text{O}}) = \nabla \cdot [\rho D_{\text{capill}} \nabla Y^{\text{H}_2\text{O}}] + S^{\text{H}_2\text{O}} \quad (16)$$

This equation explains the water is transported by capillary diffusion in the porous media with the capillary diffusivity being

$$D_{\text{capill}} = \frac{1}{\rho} (Y_l^{\text{H}_2\text{O}} - Y_g^{\text{H}_2\text{O}}) \frac{\lambda_g \lambda_l \sigma |\cos(\theta_c)| (K\epsilon)^{1/2}}{\nu} \frac{dJ}{ds} \frac{\rho_l (\rho_g Y_l^{\text{H}_2\text{O}} - \rho_g Y_g^{\text{H}_2\text{O}})}{(\rho_l Y_l^{\text{H}_2\text{O}} - \rho_l Y^{\text{H}_2\text{O}} + \rho_g Y^{\text{H}_2\text{O}} - \rho_g Y_g^{\text{H}_2\text{O}})^2} \quad (17)$$

2.5. Two-phase methanol transport equation

By assuming methanol vapor–liquid equilibrium in the anode (Henry's law), two-phase mass fraction relationship (Eq. (8)) of methanol can be reformed as follows:

$$Y^{\text{MeOH}} = \frac{\rho_l}{\rho} \left(s + \frac{1-s}{k_H} \right) Y_l^{\text{MeOH}} \quad (18)$$

By plugging Eq. (18) into Eq. (12), the methanol transport equation becomes

$$\begin{aligned} \nabla \cdot (\rho \vec{u} Y_l^{\text{MeOH}}) &= \nabla \cdot \left[\rho_l \left(D_{l,\text{eff}}^{\text{MeOH}} + \frac{D_{g,\text{eff}}^{\text{MeOH}}}{k_H} \right) \nabla \cdot Y_l^{\text{MeOH}} \right] \\ &\quad - \nabla \cdot \left[Y_l^{\text{MeOH}} \left(\frac{\rho_l}{\rho_g k_H} - 1 \right) \vec{j}_l \right] + S^{\text{MeOH}} \end{aligned} \quad (19)$$

2.6. MOR and ORR

Butler–Volmer equation is simplified as Tafel equation in this study. It is known that methanol oxidation reaction (MOR) is 0th order when the methanol concentration is high enough and 1st order when the methanol concentration approaches the depletion limit. Following equation is used to simulate a smooth transition from 0th order kinetics to 1st order kinetics in this study [7–9].

$$j = \frac{a j_{0,a}^{\text{ref}} c_l^{\text{MeOH}} \exp\left(\frac{\alpha_a F}{RT} \eta_a\right)}{c_l^{\text{MeOH}} + K_c \exp\left(\frac{\alpha_a F}{RT} \eta_a\right)} \quad [\text{A/m}^2] \quad (20)$$

where $\eta_a = \Phi_s - \Phi_e - U_a^0$ [V]

On the cathode side, oxygen reduction reaction (ORR) is assumed to be proportional to oxygen concentration.

$$j = a j_{0,c}^{\text{ref}} \left(\frac{c_{\text{O}_2}}{c_{\text{O}_2}^{\text{ref}}} \right) (1-s)^n \exp\left(-\frac{\alpha_c F}{RT} \eta_c\right) \quad [\text{A/m}^2] \quad (21)$$

where $\eta_c = \Phi_s - \Phi_e - U_c^0$ [V]

2.7. Methanol crossover rate (MCO)

Some amount of methanol that couldn't react in the anode catalyst layer may move to the cathode side by permeating the membrane. This crossover methanol can participate either in the electrochemical

reaction which produces crossover current $i_{\text{crossover}}$ or in the pure chemical reaction, i.e. combustion. Crossover current has negative effect on the cell performance since it causes mixed potential which degrades the cell performance. In addition, crossover current consumes additional fuel and oxidizer, which reduces the fuel efficiency of DMFC also. Crossover current can be described as shown in Eq. (22) [3]. It is considered that methanol electro-osmosis drag and methanol diffusion contribute to the total methanol crossover.

$$\begin{aligned} i_{\text{crossover}} &= 6FN_{\text{mem}}^{\text{MeOH}} \\ \text{where } N_{\text{mem}}^{\text{MeOH}} &= \frac{i_{\text{crossover}}}{6F} = n_d^{\text{MeOH}} \frac{i}{F} + D_{\text{mem}}^{\text{MeOH}} \frac{c_{\text{acl}}^{\text{MeOH}}}{\delta_{\text{mem}}} \end{aligned} \quad (22)$$

Methanol crossover rate (MCO) describes the fuel efficiency of a DMFC as follows [12]:

$$\text{MCO} = \frac{i_{\text{crossover}}}{i + i_{\text{crossover}}} \quad (23)$$

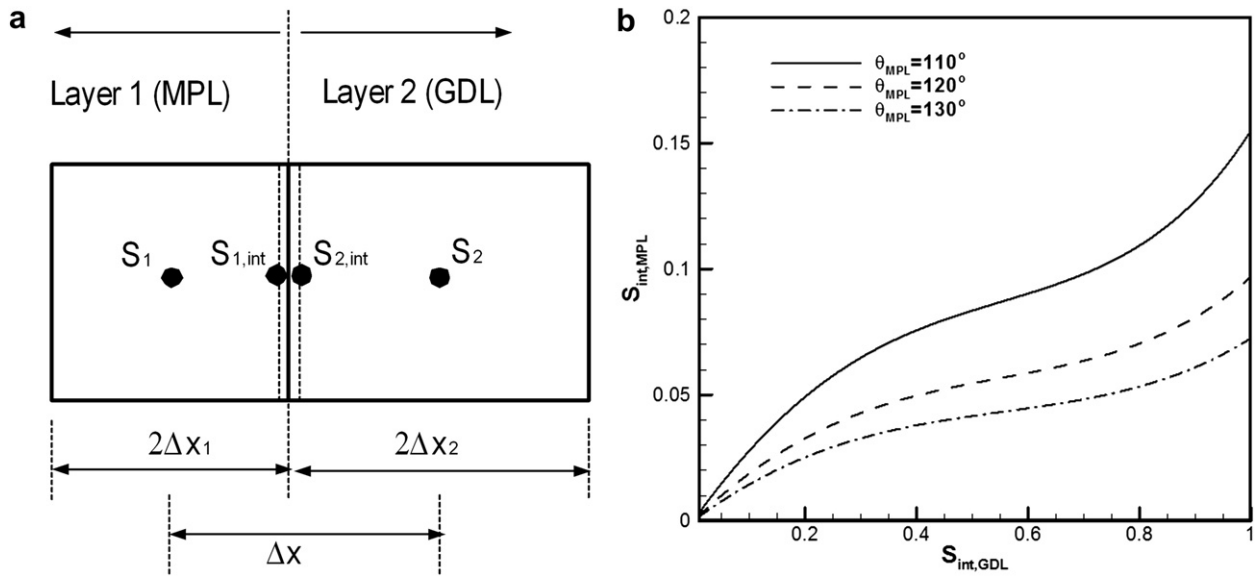


Fig. 3. Liquid saturation jump at the MPL/GDL interface: (a) Schematic of interfacial control volumes (MPL/GDL) for saturation jump, (b) Interfacial liquid saturation profiles according to θ_{mpl} (when θ_{gdl} is fixed as 100°).

2.8. Cell voltage

Generally, cell voltage is described as following equation considering overpotentials.

$$V_{cell} = (U_c^0 - \eta_c) - (U_a^0 - \eta_a) - I \cdot R_{mem} - I \cdot R_{other} \quad (24)$$

However, as the present DMFC mode simultaneously solves all the governing equations listed in Table 1, cell voltage can be sensed by the electron-phase potential value difference between anode bipolar plate and cathode bipolar plate as follows:

$$V_{cell} = \Phi_{s,CBP} - \Phi_{s,ABP} \quad (25)$$

This cell voltage includes all of overpotentials such as ohmic loss, concentration loss and kinetics loss.

2.9. Net water transfer coefficient (α)

Water is a necessary reactant in MOR. Water transport through membrane can be expressed using the net water transport coefficient defined in Eq. (26) which consists of electro-osmosis drag, diffusion and hydraulic permeation [10]. By examining the water transport coefficient, we can find out whether water is being lost or gained.

2.10. Multi-dimensional saturation jump model

Qi and Kaufman [11] experimentally showed the effect of micro-porous layer (MPL) which is inserted between GDL and catalyst layer on the water transport and distribution in fuel cells. As this MPL is made of finer and more hydrophobic materials than other porous layers, a discontinuity in the liquid saturation across the interface of two layers occurs while the liquid pressure at the interface is continuous. Anode MPL has the effect of reducing saturation level in the anode catalyst layer by blocking water flow from the anode channel whereas cathode MPL has the effect of increasing saturation level in the cathode catalyst layer by reserving produced water by ORR. Therefore, the net water flux from the anode to cathode is greatly reduced or even it negatively flows from the cathode to anode, which is helpful for water management. Nam and Kaviani [4] theoretically explained the saturation discontinuity effect with one-dimensional mathematical model, so called saturation jump model. Passaogullari and Wang [5] further investigated the effect of saturation jump with MPL on the water transport in the porous media of a fuel cell. Shaffer and Wang [12] conducted a theoretical discussion about the effect of hydrophobic MPL on the cell performance and the fuel efficiency of DMFCs by simulating one-dimensional model. In order to minimize water/methanol crossover in a DMFC, most of DMFCs recently developed have two MPLs with thin proton

$$\alpha = N_{mem,\bar{i}}^{H_2O} \frac{F}{i} = \left(N_{mem,EOD}^{H_2O} + N_{mem,diff}^{H_2O} + N_{mem,hp}^{H_2O} \right) \frac{F}{i} = n_d^{H_2O} + \alpha_{mem,diff} + \alpha_{mem,hp}$$

$$\text{where} \begin{cases} n_d^{H_2O} = N_{mem,EOD}^{H_2O} \frac{F}{i} \\ \alpha_{mem,diff} = N_{mem,diff}^{H_2O} \frac{F}{i} = D_{mem}^{H_2O} \left(\frac{\rho_{mem}}{EW_{mem}} \right) \left(\frac{\lambda_a - \lambda_c}{\delta_{mem}} \right) \frac{F}{i} \\ \alpha_{mem,hp} = N_{mem,hp}^{H_2O} \frac{F}{i} = \left(\frac{\rho_l K_{mem}}{M_l \mu_l} \right) \left(\frac{p_{l,a} - p_{l,c}}{\delta_{mem}} \right) \frac{F}{i} \end{cases} \quad (26)$$

exchange membrane, so called 'low- α MEA'. Experimental results by Liu and Wang [13] showed that the cell performance and fuel efficiency can be greatly improved with properly selected MPLs in the anode and cathode. As Nam and Kaviany [4] and Shaffer and Wang [12]'s one-dimensional model directly solved flux-based liquid saturation equation with above relationship, their model easily shows a saturation profile in through-plane direction. However, as the present multi-dimensional model solves mass fraction equation instead of saturation equation, saturation distribution is acquired from mass fraction distribution in Eq. (7). Furthermore, several parameters and constitutive relationships of the multi-dimensional model depend on saturation distribution, which means saturation and mass fractions are strongly coupled in the model. We introduce how to implement saturation jump in the present multi-dimensional DMFC model. Fig. 3(a) shows the interface of two different porous layers (GDL and MPL). As the capillary pressure should be continuous at this interface as follows:

$$\sigma \cos \theta_{c,1} \left(\frac{\varepsilon_1}{K_1} \right) J(s_{1,int}) = \sigma \cos \theta_{c,2} \left(\frac{\varepsilon_2}{K_2} \right) J(s_{2,int}) \quad (27)$$

When the saturation of one layer is given, the saturation of the other layer can be found by solving following equation. Calculation result is shown in Fig. 3(b).

$$J(s_{1,int}) = \frac{\beta_2}{\beta_1} J(s_{2,int}) \quad \text{where} \quad \begin{cases} \beta_1 = \sigma \cos(\theta_1) \left(\frac{\varepsilon_1}{K_1} \right)^{1/2} \\ \beta_2 = \sigma \cos(\theta_2) \left(\frac{\varepsilon_2}{K_2} \right)^{1/2} \end{cases} \quad (28)$$

However, the multi-dimensional model calculates liquid saturation in each mesh (s_1 and s_2) and interfacial liquid saturation (s_{int}) is not given. Therefore, interfacial liquid saturation should be determined by s_1 and s_2 by water flux continuity (liquid phase and vapor phase) at the mesh interface as follows:

$$N_{int} = N_{1,int} = N_{2,int} \\ D_{s,1} \frac{s_{1,int} - s_1}{\Delta x_1} + D_{g,1} \frac{c_{g,int} - c_{g,1}}{\Delta x_1} = D_{s,2} \frac{s_2 - s_{2,int}}{\Delta x_2} + D_{g,2} \frac{c_{g,2} - c_{g,int}}{\Delta x_2} \quad (29)$$

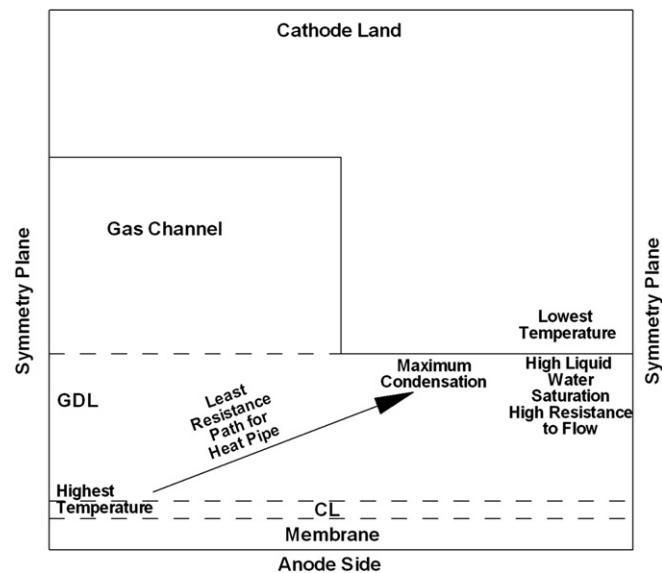


Fig. 4. Schematic of heat-pipe effect in a PEMFC [14].

Then from Eq. (29), we have,

$$s_{2,int} = A \cdot s_{1,int} + B \quad (30)$$

where

$$A = \frac{D_{s,1} \Delta x_2}{D_{s,2} \Delta x_1} \\ B = \left(D_{s,1} \frac{s_1}{\Delta x_1} + D_{s,2} \frac{s_2}{\Delta x_2} - f_{g,1} + f_{g,2} \right) \frac{\Delta x_2}{D_{s,2}} \\ f_{g,1} = D_{g,1} \frac{c_{g,int} - c_{g,1}}{\Delta x_1} \\ f_{g,2} = D_{g,2} \frac{c_{g,2} - c_{g,int}}{\Delta x_2}$$

Now we combine Eq. (28) and Eq. (30) to get interfacial liquid saturation and interfacial liquid flux. Interfacial liquid saturation does not explicitly show up in the multi-dimensional model. Instead, we add or subtract interfacial liquid flux found above in the mesh 1 and 2 as follows:

$$S_1 = -\nabla \cdot \left(\rho D_{capill} \nabla Y^{H_2O} \right) + M^{H_2O} \nabla \cdot N_{int} \\ S_2 = -\nabla \cdot \left(\rho D_{capill} \nabla Y^{H_2O} \right) - M^{H_2O} \nabla \cdot N_{int} \quad (31)$$

Finally, above water source term is put to the water equation of Eq. (16).

2.11. Two-phase heat transfer model

As liquid water and water vapor coexist in a DMFC, water concentration is strongly affected by temperature whereas temperature is affected by the latent heat due to the water phase change (condensation and evaporation). Therefore, species equation and energy equation are strongly coupled in the present multi-dimensional model. Standard energy equation for the present DMFC model is derived from M² model [6].

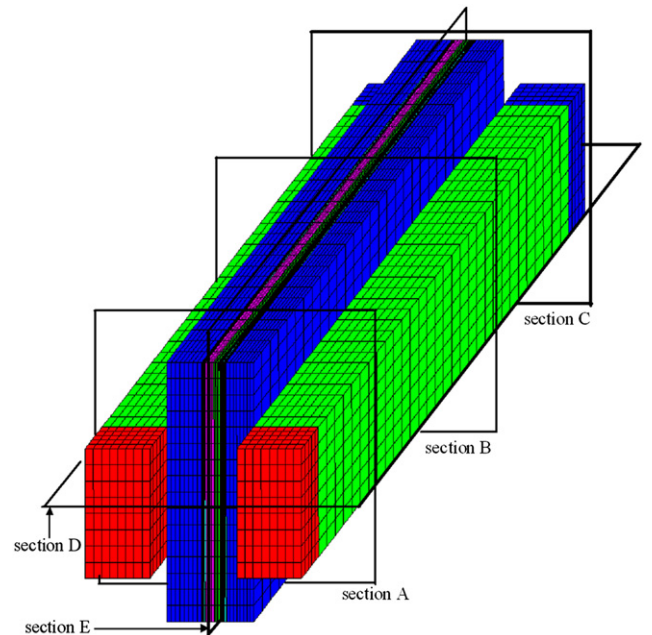


Fig. 5. Three-dimensional mesh of the single channel DMFC model for the present study.

Table 3

Cell geometry and material properties of the baseline DMFC model.

Description	Symbol	Value
Anode GDL thickness	δ_{adl}	270 μm
Anode MPL thickness	δ_{aml}	30 μm
Anode CL thickness	δ_{acl}	62 μm
Membrane thickness	δ_{mem}	45 μm
Cathode CL thickness	δ_{ccl}	25 μm
Cathode MPL thickness	δ_{cml}	30 μm
Cathode GDL thickness	δ_{cdl}	210 μm
GDL porosity	ε_{gdl}	0.6
MPL porosity	ε_{mpl}	0.4
CL porosity	ε_{cl}	0.4
FD porosity	ε_{fd}	0.3
GDL permeability	K_{gdl}	$2.0 \times 10^{-12} \text{ m}^2$
MPL permeability	K_{mpl}	$5.0 \times 10^{-14} \text{ m}^2$
CL permeability	K_{cl}	$1.0 \times 10^{-13} \text{ m}^2$
FD permeability	K_{fd}	$2.84 \times 10^{-13} \text{ m}^2$
Membrane permeability	K_{mem}	$4.0 \times 10^{-20} \text{ m}^2$
GDL contact angel	θ_{gdl}	110°
MPL contact angel	θ_{mpl}	114°
CL contact angle	θ_{cl}	96°
Cell length	L_{cell}	75 mm
Channel width	W_{chan}	1 mm
Channel height	H_{chan}	0.5 mm
Land width	W_{land}	1 mm
Bipolar plate thickness	H_{bp}	0.5 mm

$$\nabla \cdot (\rho c_p \vec{u} T) = \nabla \cdot (k \nabla T) + S^T$$

where $S^T = S_{sensible}^T + S_{latent}^T$ (32)

There are three sensible heat source terms in the anode: 1) irreversible heat of the electrochemical reaction, 2) reversible entropic heat, 3) ohmic heating, respectively (see Eq. (33)). In the membrane, only ohmic heating exists since electrochemical reaction does not occur there.

$$S_{sensible,acl}^T = j \left(\eta + T \frac{dU^0}{dT} \right) + \frac{i^2}{\kappa_{eff}}$$

$$S_{sensible,mem}^T = \frac{i^2}{\kappa_{eff}}$$

$$S_{sensible,ccl}^T = j \left(\eta + T \frac{dU^0}{dT} \right) + j_{xover} \left(\eta + T \frac{dU^0}{dT} \right) + \frac{i^2}{\kappa_{eff}}$$

(33)

The influence of methanol crossover on energy balance is added also, which generates additional heat in the cathode catalyst layer where crossovered methanol reacts. Latent heat effect is included in the present model as following equation.

$$S_{latent}^T = \dot{m}_{fg} h_{fg}^0 = \nabla \cdot (h_{fg}^0 \rho_l \vec{u}_l)$$

$$= \nabla \cdot \left(h_{fg}^0 \frac{\lambda_l \lambda_g \sigma \cos(\theta_c)}{\nu} (K_E)^{1/2} \frac{dJ}{ds} \nabla s - h_{fg}^0 \lambda_l \frac{K}{\nu} \nabla p \right)$$

(where \dot{m}_{fg} is the phase – changing rate) (34)

Table 4

Simulation parameters and operating conditions of the baseline DMFC model.

Description	Symbol	Value
Reference current density	i_{ref}	150 mA cm^{-2}
Anode reference exchange current density	i_a^0	45.51 A m^{-2}
Cathode reference exchange current density	i_c^0	0.12 A m^{-2}
Anode catalyst ionomer		25 vol.%
Cathode catalyst ionomer		25 vol.%
Anode catalyst loading		4 mg cm^{-2}
Cathode catalyst loading		2 mg cm^{-2}
Surface tension	σ	0.0625 N m^{-1}
Inlet methanol concentration	$C_{MeOH,in}$	4000 mol m^{-3}
Pure liquid methanol concentration	$C_{MeOH,pure}$	24,719 mol m^{-3}
Pure liquid water concentration	$C_{H_2O,pure}$	55,556 mol m^{-3}
Total anode transfer coefficients	α_a	0.239
Total cathode transfer coefficients	α_c	0.875
Faraday constant	F	96,487 C mol^{-1}
Universal gas constant	R	8.314 $\text{J mol}^{-1} \text{K}$
Equivalent weight of dry membrane	EW	1.1 kg mol^{-1}
Dry membrane density	ρ_{dry}	1980 kg m^{-3}
Cell temperature	T_{cell}	313 K
Anode stoichiometry	ξ_a	1.4
Cathode stoichiometry	ξ_c	2.0
Operating current density	i_{avg}	150 mA cm^{-2}

This source term arises from latent heat release or absorption due to water condensation/evaporation in two-phase flow region. Evaporation occurs in the near surface area of GDL where air flow carries moist away. Condensation occurs in the cold region (under the land region) and cathode catalyst layer region where water is being produced by ORR. Because the present model assumes water is produced first in the vapor form, excessive water which is greater than the saturation value must be condensed as liquid form.

2.12. Non-isothermal behavior: the heat-pipe effect

In a typical DMFC, heat transfer in the anode is mostly carried out by liquid flow in the channel which has large convective heat transfer coefficient (liquid cooling). However, in the cathode, heat conduction and heat-pipe effect are important since there is no liquid flow. Basu et al. [14] investigated the phase change and heat-pipe effect in a hydrogen PEMFC (proton exchange membrane fuel cell). They showed the cell operating condition (relative humidity of the inlet gas) and material property (heat conductivity of GDL) have a strong influence on the phase change and temperature distribution by quantifying the phase-changing rate and the portion of heat transfer by heat-pipe effect. In this part, we reproduce the non-isothermal behavior with the heat-pipe effect in a DMFC by adopting Basu's methodology.

Fig. 4 shows how heat transfer occurs in the cathode by heat-pipe effect. As the catalyst layer is hottest due to reaction and land is coldest, major heat flow direction is from the catalyst to GDL/land interface. Water vapor near the catalyst layer is transported to GDL/land interface by thermal diffusion and it condenses there due to lower temperature. Condensed water near GDL/land interface moves toward the gas channel and finally it evaporates since dry air flow carries moist away. By considering heat balance near GDL/land interface, following result can be derived:

$$\frac{d}{dx} \left[\left(k_{gdl} + h_{fg}^0 M^{H_2O} D_{g,eff} \frac{dc_{sat}^{H_2O}}{dT} \right) \frac{dT}{dx} \right] = \frac{d}{dx} \left(k_{eff} \frac{dT}{dx} \right)$$

where $\begin{cases} D_{g,eff}^{H_2O} = D_{g,s}^{H_2O} (1-s)^{2.3} \varepsilon^4 : \text{Effective water vapor diffusivity} \\ k_{eff} = k_{gdl} + h_{fg}^0 M^{H_2O} D_{g,eff} \frac{dc_{sat}^{H_2O}}{dT} : \text{Effective thermal conductivity} \end{cases}$ (35)

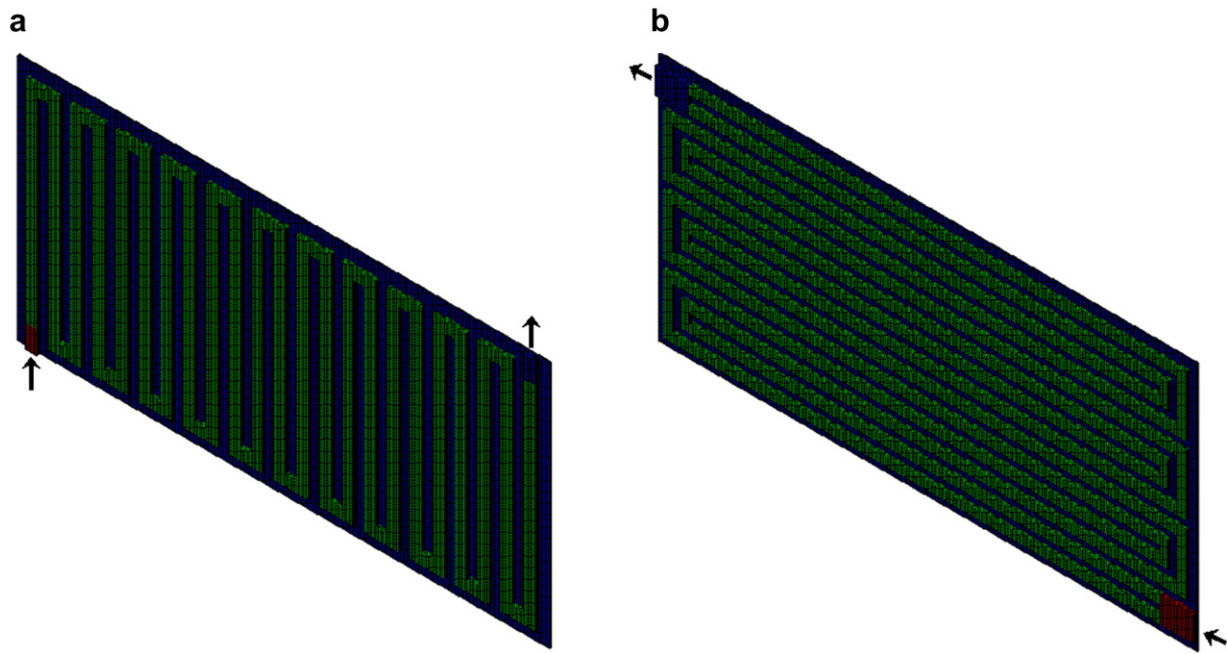


Fig. 6. Three-dimensional mesh of the full-scale DMFC model (28 cm²) which has serpentine channel configuration for the present study: (a) anode mesh, (b) cathode mesh.

Above result implies that the heat-pipe effect increases the effective thermal conductivity, which improves heat release.

In addition to the heat transfer effect, heat-pipe effect includes water transport effect also. When the cell is non-isothermal, thermal vapor diffusion occurs due to water vapor concentration

gradient in the two-phase region. As this thermal vapor diffusion occurs from hot to cold region, liquid saturation in the hot region decreases and it increases in the cold region, which means water removal from the cathode porous media to the cathode channel is enhanced. As water is transported by both capillary diffusion and

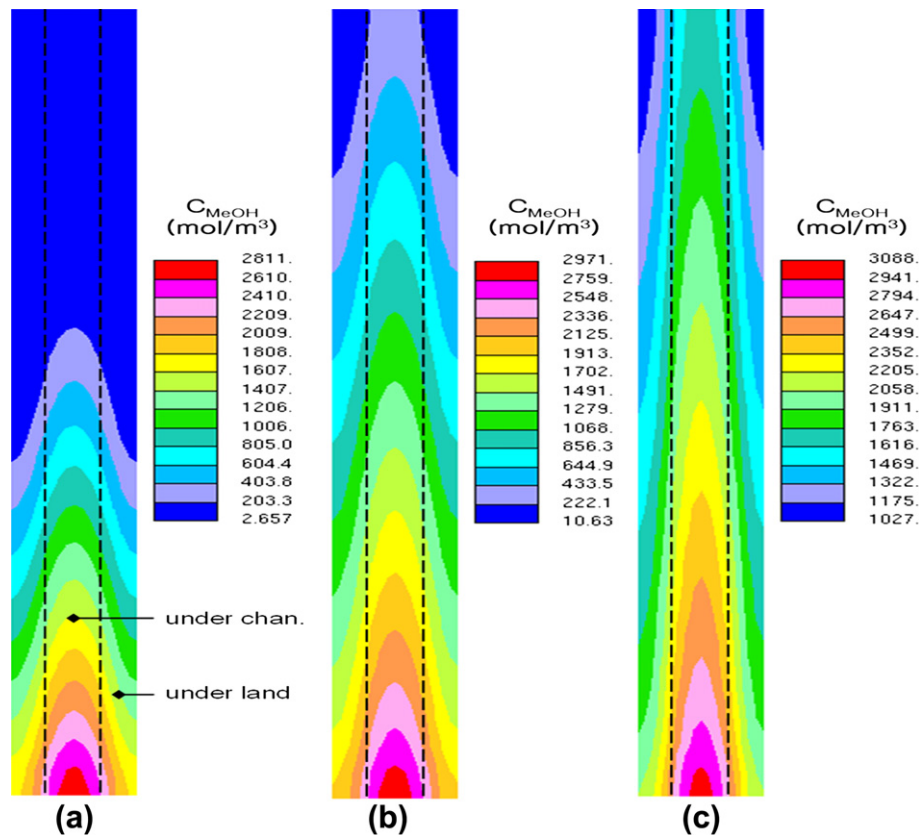


Fig. 7. Methanol concentration in the anode catalyst layer of the single channel cell model according to the flow stoichiometry: (left) $T_{cell} = 313$ K, $\zeta_a = 1.4$, $\zeta_c = 2.0$, (center) $T_{cell} = 313$ K, $\zeta_a = 2.4$, $\zeta_c = 2.4$, (right) $T_{cell} = 313$ K, $\zeta_a = 5.0$, $\zeta_c = 5.0$.

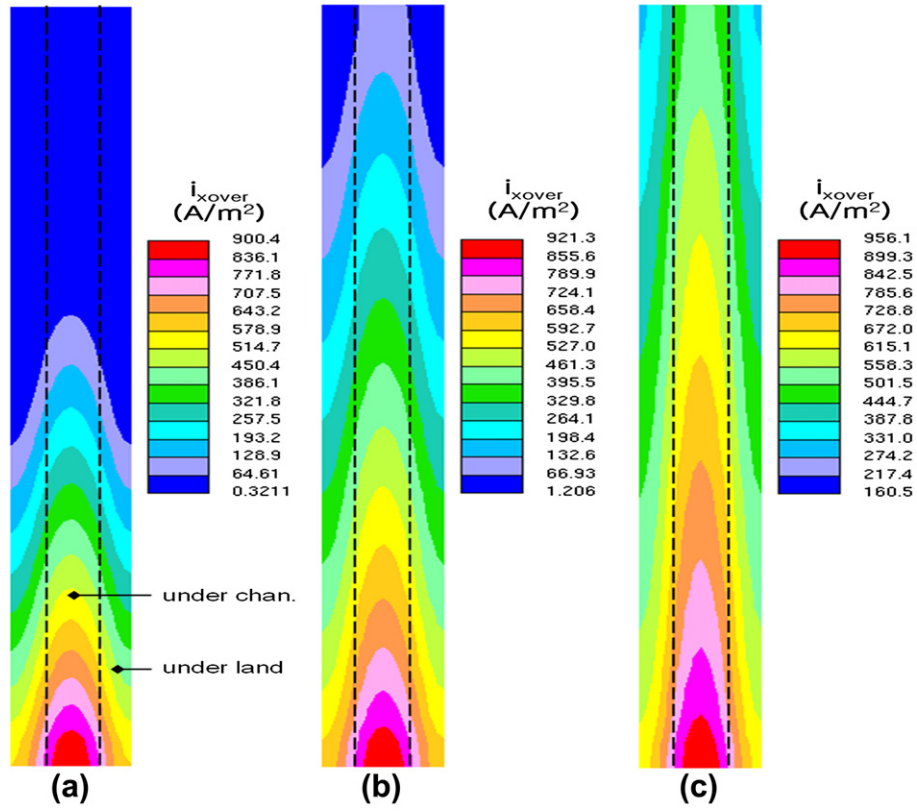


Fig. 8. Crossover current density distribution of the single channel cell model according to the flow stoichiometry: (left) $T_{\text{cell}} = 313 \text{ K}$, $\zeta_a = 1.4$, $\zeta_c = 2.0$, (center) $T_{\text{cell}} = 313 \text{ K}$, $\zeta_a = 2.4$, $\zeta_c = 2.4$, (right) $T_{\text{cell}} = 313 \text{ K}$, $\zeta_a = 5.0$, $\zeta_c = 5.0$.

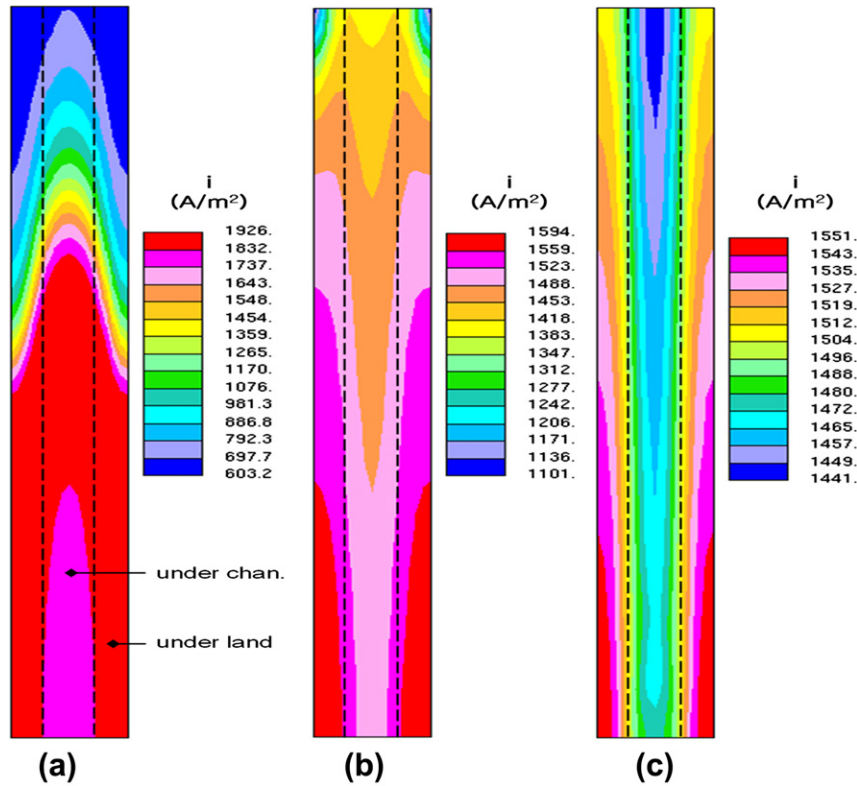


Fig. 9. Current density distribution of the single channel cell model according to the flow stoichiometry: (left) $T_{\text{cell}} = 313 \text{ K}$, $\zeta_a = 1.4$, $\zeta_c = 2.0$, (center) $T_{\text{cell}} = 313 \text{ K}$, $\zeta_a = 2.4$, $\zeta_c = 2.4$, (right) $T_{\text{cell}} = 313 \text{ K}$, $\zeta_a = 5.0$, $\zeta_c = 5.0$.

non-isothermal vapor diffusion in the two-phase region, we can expect the net water transfer coefficient will increase. Contrary to the heat equation, those two water transport mechanism (capillary diffusion and thermal vapor diffusion) are not compatible. Hence, they cannot be incorporated in a single diffusion term. Therefore, we introduce an additional water source term to reflect the thermal vapor diffusion as follows:

$$S_{diff}^{H_2O} = \int_V \nabla \cdot [\bar{D}_{g,eff}^{H_2O} Y_{H_2O}^{H_2O}(T)] \quad (36)$$

This term is added to the water equation Eq. (16).

2.13. Full-scale DMFC model with parallel channel configuration

Fig. 5 shows the mesh used for the present multi-dimensional DMFC modeling, which simulates a single channel (75 mm length) of a 28 cm² DMFC which has 18 parallel channels. In order to save computational time, we assume every single channel is identical in the parallel cell configuration without any channel clogging by CO₂ bubbles. Therefore, this single channel can be considered to represent the entire DMFC cell area. Cell specification and simulation parameters are listed in Tables 3 and 4, respectively.

2.14. Full-scale DMFC model with serpentine channel configuration

Many DMFCs adopt serpentine channel configuration in order to avoid channel clogging problem although serpentine channel causes larger pressure drop than the parallel configuration. On the cathode side, removed water from the GDL surface may condense in the cathode channel, which may clog the channel and hinder air supply although it is not so much severe as the anode side since a typical DMFC operates at low current compared to hydrogen PEMFC (water production is almost 1/10). Therefore, DMFC with serpentine channel configuration will have non-uniform distribution of species, current and temperature compared to DMFC with parallel channel configuration.

Fig. 6 shows 3-D mesh of the full-scale DMFC model (28 cm²). Anode has single-pass serpentine channel in order to sweep away CO₂ bubbles whereas cathode has two-pass serpentine channel. As volumetric air flow rate is much larger than liquid fuel flow rate, pressure drop in the cathode channel is much greater than that of the anode channel. In order to reduce pressure drop due to this large air flow rate, 2–4 serpentine passes are arranged to grasp both reduced pressure drop and better removal of water droplets. Anode channel and cathode channel are arranged as cross-flow configuration in order to minimize non-reactive area and promote uniform distribution of fuel and oxygen.

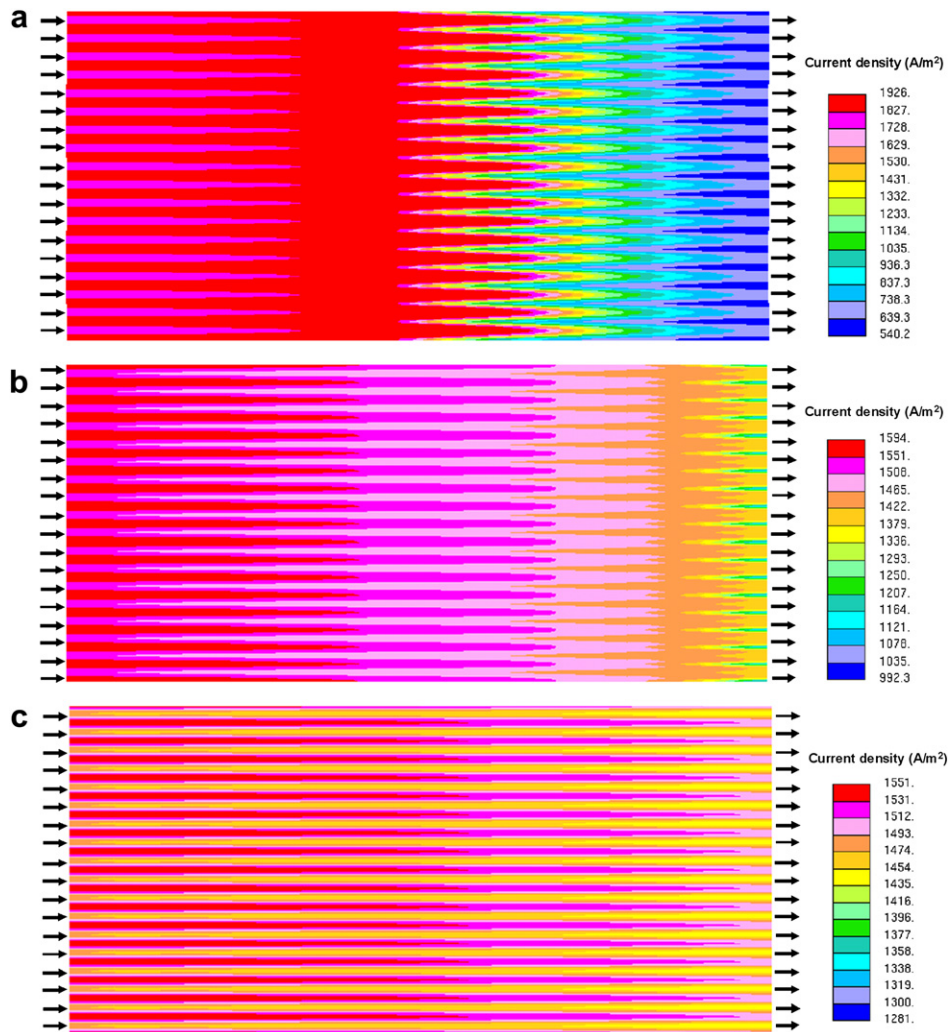


Fig. 10. Current density distribution in the cell with parallel channel configuration according to the flow stoichiometry: (a) $T_{cell} = 313$ K, $\zeta_a = 1.4$, $\zeta_c = 2.0$, (b) $T_{cell} = 313$ K, $\zeta_a = 2.4$, $\zeta_c = 2.4$, (c) $T_{cell} = 313$ K, $\zeta_a = 5.0$, $\zeta_c = 5.0$.

Table 5
Effect of flow stoichiometry on the cell performance (single channel model).

	T_{cell} (K)	RH (%)	C_{MeOH} (M)	ζ_a	ζ_c	i (mA cm ⁻²)	V_{cell} (V)	MCO (%)
Case A	313.0	10.0	4.0	1.4	2.0	150	0.409	12.0
Case B	313.0	10.0	4.0	2.4	2.4	150	0.455	19.1
Case C	313.0	10.0	4.0	5.0	5.0	150	0.461	28.1

2.15. Implementation

Present mathematical model is implemented into a commercial CFD solver STAR-CDTM with user subroutine capability. It is considered the convergence is achieved when the residuals reach 10^{-6} . Parallel computing is used for the full-scale simulation.

3. Results and discussion

3.1. Parallel channel configuration

3.1.1. Effect of flow stoichiometry on the cell performance and fuel efficiency

As the flow stoichiometry (or flow-rate) increases, methanol concentration in the anode increases also as shown in Fig. 7. Under the channel region has higher methanol concentration than under

the land region due to the short diffusion length. As defined in Eq. (22), crossover current density is strongly affected by the methanol concentration near membrane/ACL interface. Therefore, crossover current density distribution is similar to that of methanol concentration as shown in Fig. 8.

Fig. 9 shows the current density distribution in a single channel model according to the fuel stoichiometry. When fuel supply is large enough, current density is uniformly distributed in the flow stream direction as shown Fig. 9(c) and the highest current density is observed under the land region. In a DMFC, when methanol supply is large enough, MOR is 0th order, which means MOR is not so much affected by the methanol concentration in the anode catalyst layer. However, excessive methanol transported to the cathode side (under the channel region) degrades the cell performance by producing mixed potential, which results in lower current density under the channel region where methanol crossover is high. When fuel stoichiometry is low, MOR is affected by the methanol concentration in the anode catalyst layer and the highest current density is observed under the channel region as shown in Fig. 9(a). If fuel supply is intermediate, the highest current density shows up under the land in the inlet region and it is observed under the channel in the outlet region as shown in Fig. 9(b). Although large stoichiometry produces better cell performance, the fuel efficiency decreases due to large MCO. In addition, operating a cell with large stoichiometry requires much pumping power (parasite loss). Contrarily, too low

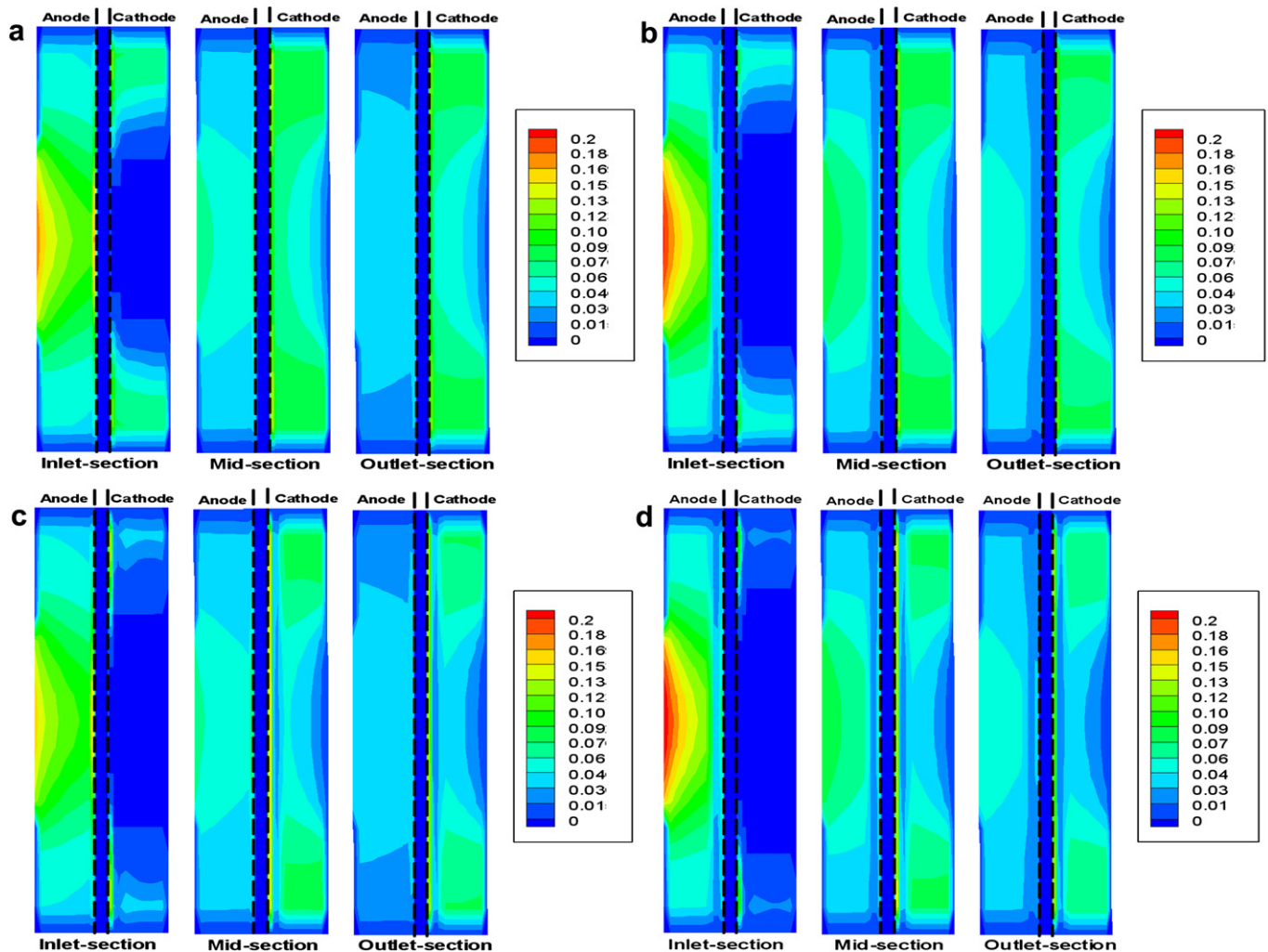


Fig. 11. Liquid saturation distribution at the cross-section A, B, C: (a) no MPL, (b) anode MPL only, (c) cathode MPL only, (d) anode and cathode MPLs.

Table 6
Effect of MPL on the cell performance (single channel model).

	Anode MPL	Cathode MPL	T_{cell} (K)	RH (%)	C_{MeOH} (M)	i (mA cm ⁻²)	ζ_a	ζ_c	V_{cell} (V)	Alpha	MCO (%)
Case A	NO	NO	333.0	90.0	2.0	150.0	3.0	3.0	0.399	0.61	0.25
Case B	YES	NO	333.0	90.0	2.0	150.0	3.0	3.0	0.407	-0.08	0.20
Case C	NO	YES	333.0	90.0	2.0	150.0	3.0	3.0	0.400	0.55	0.25
Case D	YES	YES	333.0	90.0	2.0	150.0	3.0	3.0	0.407	-0.20	0.20

stoichiometry may lead to large local concentration overpotential due to anode non-uniformity which significantly degrades the cell performance although the fuel efficiency is good and the parasitic loss is minimal.

Finally, Fig. 10 shows the current density distribution on the entire cell area that we can expect when every single channel is identical. Parallel, strip-shaped distribution is observed due to the channel configuration. Again, large flow stoichiometry results in more uniform distribution of current density. Calculation results about stoichiometry effect are summarized in Table 5.

3.1.2. Liquid saturation distribution and effect of MPL

Fig. 11 shows liquid saturation distribution in the cell cross-section according to the MPL configuration. Anode porous

media is gradually getting gaseous in the channel direction since produced CO₂ gas accumulates whereas cathode porous media becomes wetter since produced water accumulates. In the anode, the region under the channel is wetter than the region under the land. This is because CO₂ removal is blocked by the land and the region under the channel directly faces liquid flow in the channel. Contrarily, the region under the land on the cathode side is wetter than the region under the channel since liquid water removal from the cathode catalyst layer to the cathode channel is blocked there. Therefore, it is expected that net water transfer coefficient will be positive under the channel and negative (or small) under the land. When there are no MPLs, two weak saturation jumps are observed at CL/GDL interface as shown in Fig. 11(a).

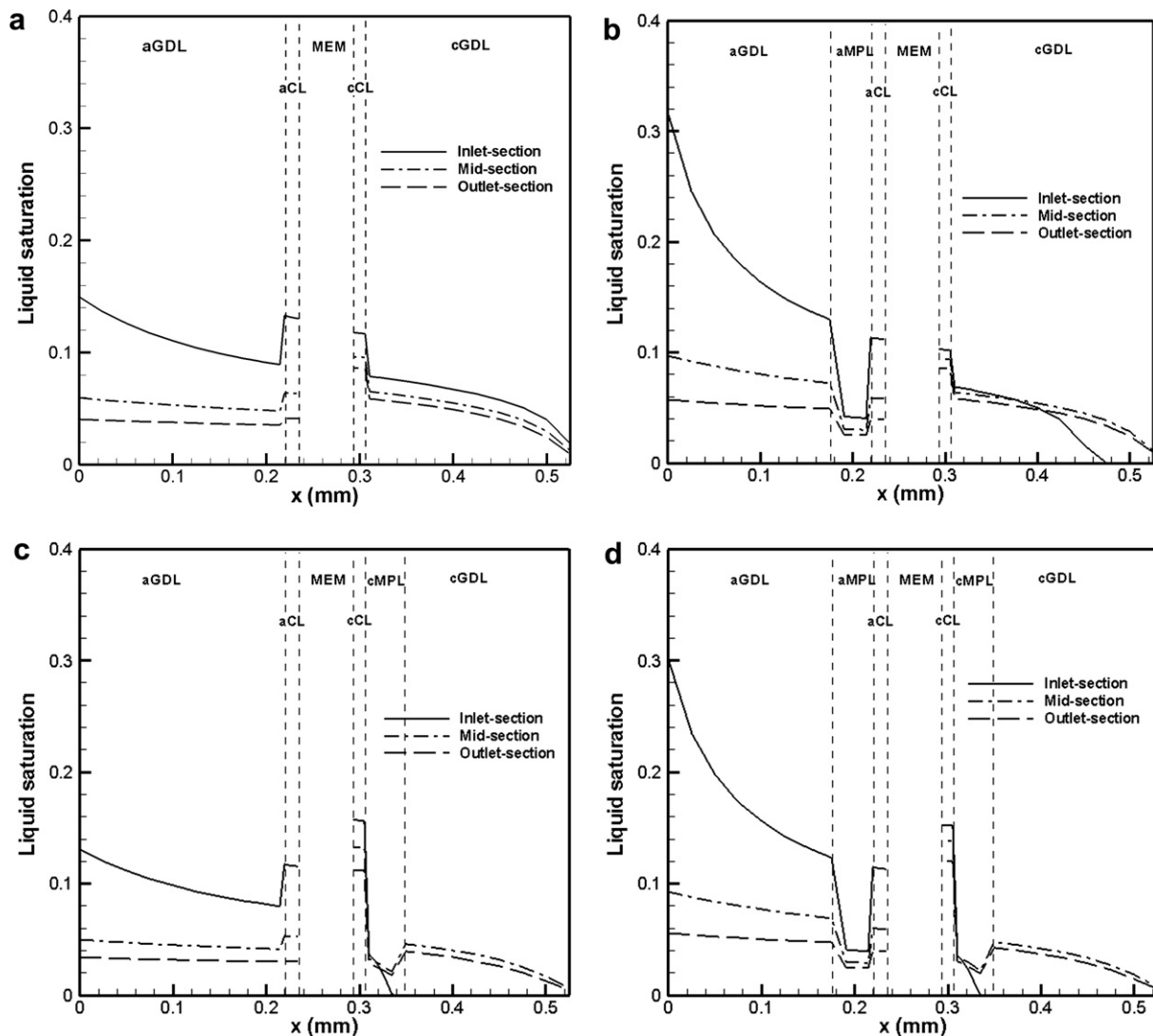


Fig. 12. Liquid saturation profile under the channel at the cross-section A, B, C: (a) no MPL, (b) anode MPL only, (c) cathode MPL only, (d) anode and cathode MPLs.

When the anode MPL is inserted between the anode GDL and the anode catalyst layer, we can see a strong saturation jump at the interface between the anode MPL and the anode catalyst layer, which effectively blocks liquid flow from the anode GDL to the anode catalyst layer and lowers the net water transfer to the cathode (see Fig. 11(b)). In addition, the anode MPL plays as a methanol transport barrier which reduces methanol concentration in the anode catalyst layer and lowers methanol crossover.

Fig. 11(c) shows the effect of the cathode MPL inserted between the cathode catalyst layer and the cathode GDL. By reserving liquid water in the cathode catalyst layer, the cathode MPL builds up hydraulic pressure and increases water back-diffusion to the anode side, which lowers the net water transfer coefficient also. Three saturation jumps are observed in this case. Note that liquid saturation in the cathode catalyst layer is especially increased. Cathode MPL does not have the effect reducing methanol crossover (Table 6).

When a cell has MPL on the anode and the cathode side, four saturation jumps can be observed as shown in Fig. 11(d). Performance comparison according to the MPL configuration is summarized in Table 6. Both MPL has the effect to lower water crossover

but only anode MPL has additional effect to lower methanol crossover. Case D which has two MPLs shows the lowest water/methanol crossover.

Figs. 12 and 13 show the effect of MPL in a different viewpoint as a form of saturation profile. Saturation jumps are more clearly noticed. When the cathode MPL is inserted, liquid saturation level in the cathode GDL is lowered due to the increased water back-diffusion. This may result in wet-to-dry transition near outlet region as shown in Fig. 12(c) and (d).

3.1.3. Effect of the thermal diffusion and phase-change on heat and water management

Fig. 14(a) and (b) compares temperature distribution and thermal diffusion rate in the cathode according to the heat conductivity of the cathode GDL. Low heat conductivity of GDL (Fig. 14(a)) results in higher temperature difference than high heat conductivity case (Fig. 14(b)). This high temperature difference drives much more water thermal diffusion from the hot region (near the cathode catalyst layer) to the cold region (GDL/CBP interface region). Note negative value denotes water is being lost whereas positive value denotes water is being supplied there. The water transported to the region GDL/CBP interface is carried away

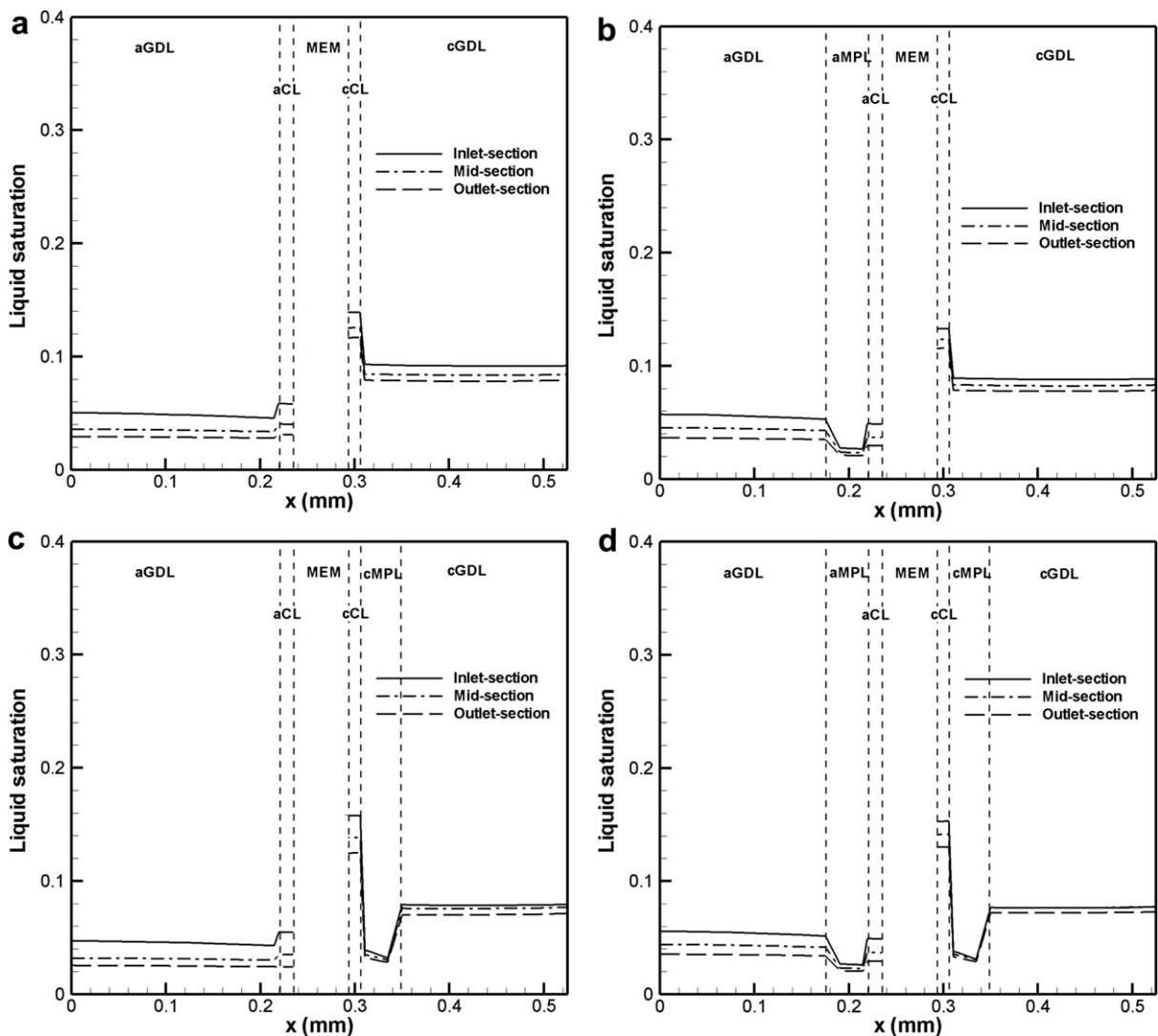


Fig. 13. Liquid saturation profile under the land at the cross-section A, B, C: (a) no MPL, (b) anode MPL only, (c) cathode MPL only, (d) anode and cathode MPLs.

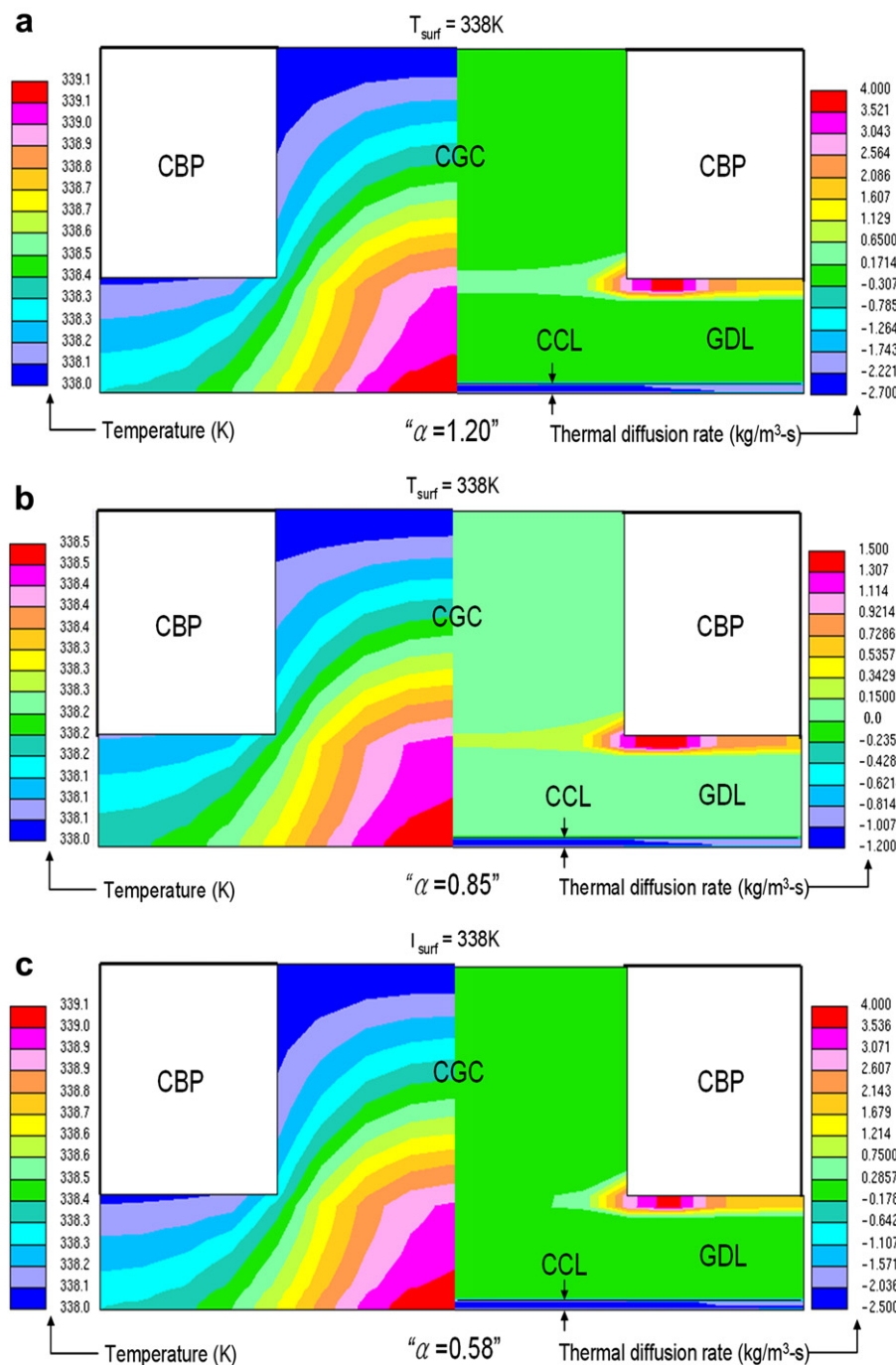


Fig. 14. Thermal diffusion rate in the cathode: (a) $k_{gdl} = 1.0 \text{ W m}^{-1} \text{ K}$, $RH = 30\%$, (b) $k_{gdl} = 3.0 \text{ W m}^{-1} \text{ K}$, $RH = 30\%$, (c) $k_{gdl} = 1.0 \text{ W m}^{-1} \text{ K}$, $RH = 70\%$.

by the air flowing through the cathode channel. As the higher temperature difference causes much more water transport (higher net water transfer coefficient value), it can be concluded that low GDL heat conductivity leads to higher net water transfer coefficient (α). Effect of supply air humidity on the thermal diffusion rate is presented by Fig. 14(a) and (c). When highly humidified air is flowing in the cathode channel (CGC), less thermal diffusion occurs due to the reduced water concentration difference. Therefore, less water is transported from CCL to CGC, which results in lower net water transfer coefficient value ($\alpha = 0.58$) compared to the dry air

case ($RH = 10\%$) that induces more water to the cathode side ($\alpha = 1.20$).

The phase-change rate is presented in Fig. 15. Positive value denotes condensation whereas negative value denotes evaporation. Water vapor transported from the cathode catalyst layer to CBP/GDL interface by thermal diffusion condenses and it moves toward the cathode channel and evaporates. Phase-change rate is affected by both material property (heat conductivity) and operating condition (relative humidity). When heat conductivity is low (Fig. 15(a)) more water condenses at CBP/GDL interface and

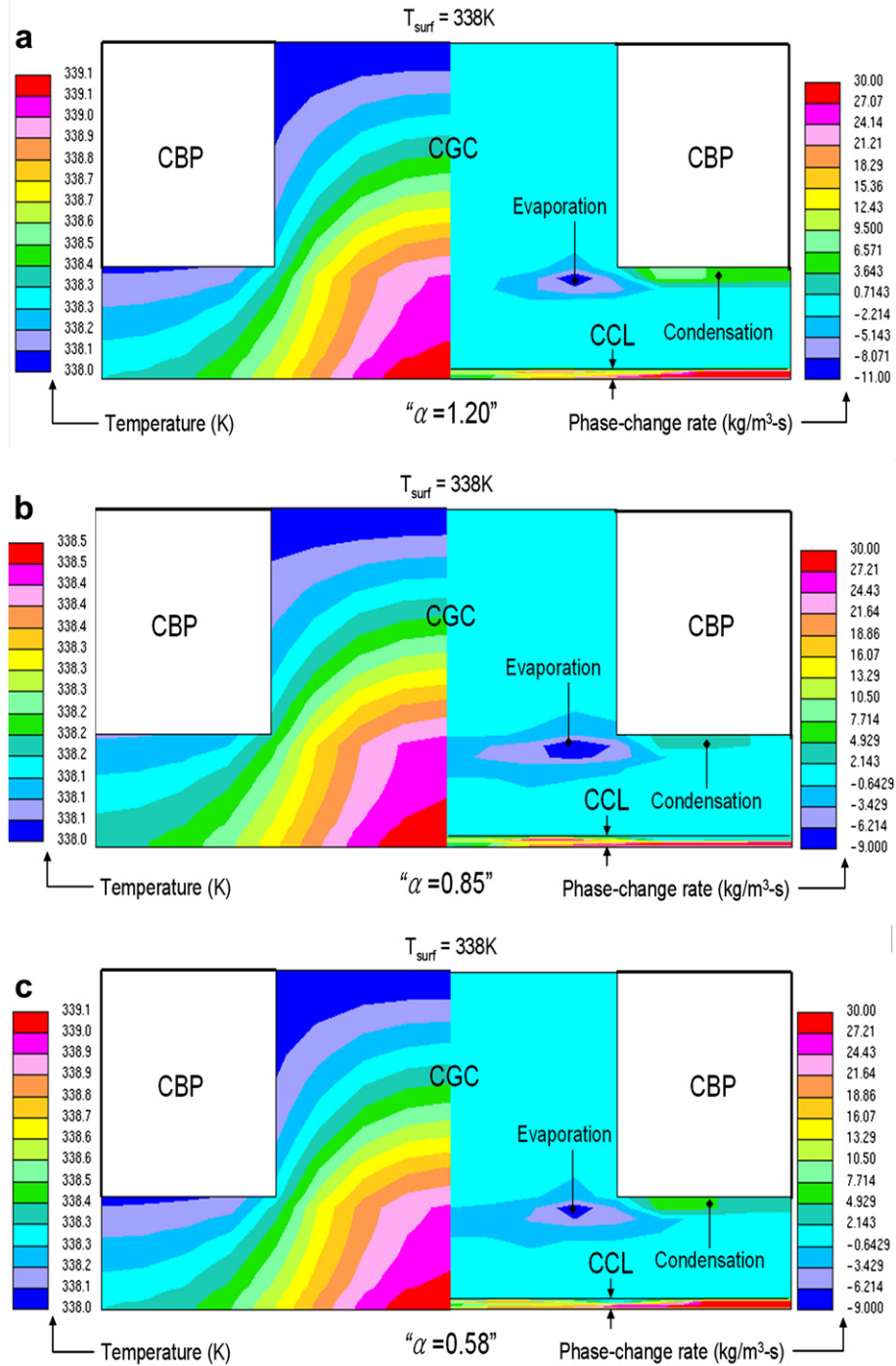


Fig. 15. Temperature and phase-change rate in the cathode: (a) $k_{gdl} = 1.0 \text{ W m}^{-1} \text{ K}$, $RH = 30\%$, (b) $k_{gdl} = 3.0 \text{ W m}^{-1} \text{ K}$, $RH = 30\%$, (c) $k_{gdl} = 1.0 \text{ W m}^{-1} \text{ K}$, $RH = 70\%$.

evaporates at CGC/GDL interface compared to the high heat conductivity case (Fig. 15(b)) since more water is transported by increased temperature difference with low heat conductivity. Effect of supply air humidity on the phase-change rate is presented by Fig. 15(a) and (c). Increased relative humidity of the air flowing in the channel results in higher liquid saturation and lowered saturation gradient in the cathode porous media, which leads to lowered phase-change rate (see Eq. (34)). From this, we can see heat and water transport are strongly coupled by both material property (heat conductivity) and cell operating condition (temperature and humidity).

Table 7

Calculation summary of full-scale DFMC simulation with serpentine channels (28 cm^2).

	$T_{cell} \text{ (K)}$	$RH \text{ (%)}$	$C_{MeOH} \text{ (M)}$	ζ_a	ζ_c	$i \text{ (mA cm}^{-2}\text{)}$	$V_{cell} \text{ (V)}$	MCO (%)
Case A	313.0	10.0	4.0	2.0	2.0	150.0	0.459	13.7
Case B	313.0	10.0	4.0	1.4	2.0	150.0	0.428	9.2
Case C	313.0	10.0	4.0	2.0	5.0	150.0	0.466	14.4

3.2. Serpentine channel configuration (28 cm^2 cell)

In order to see the effect of flow stoichiometry, three cases are simulated. Simulation conditions are listed in Table 7.

3.2.1. Methanol concentration and crossover current distribution

Fig. 16 shows methanol concentration distribution in the anode catalyst layer. Case B ($\xi_a = 1.4$) shows severe non-uniform distribution of methanol concentration, which

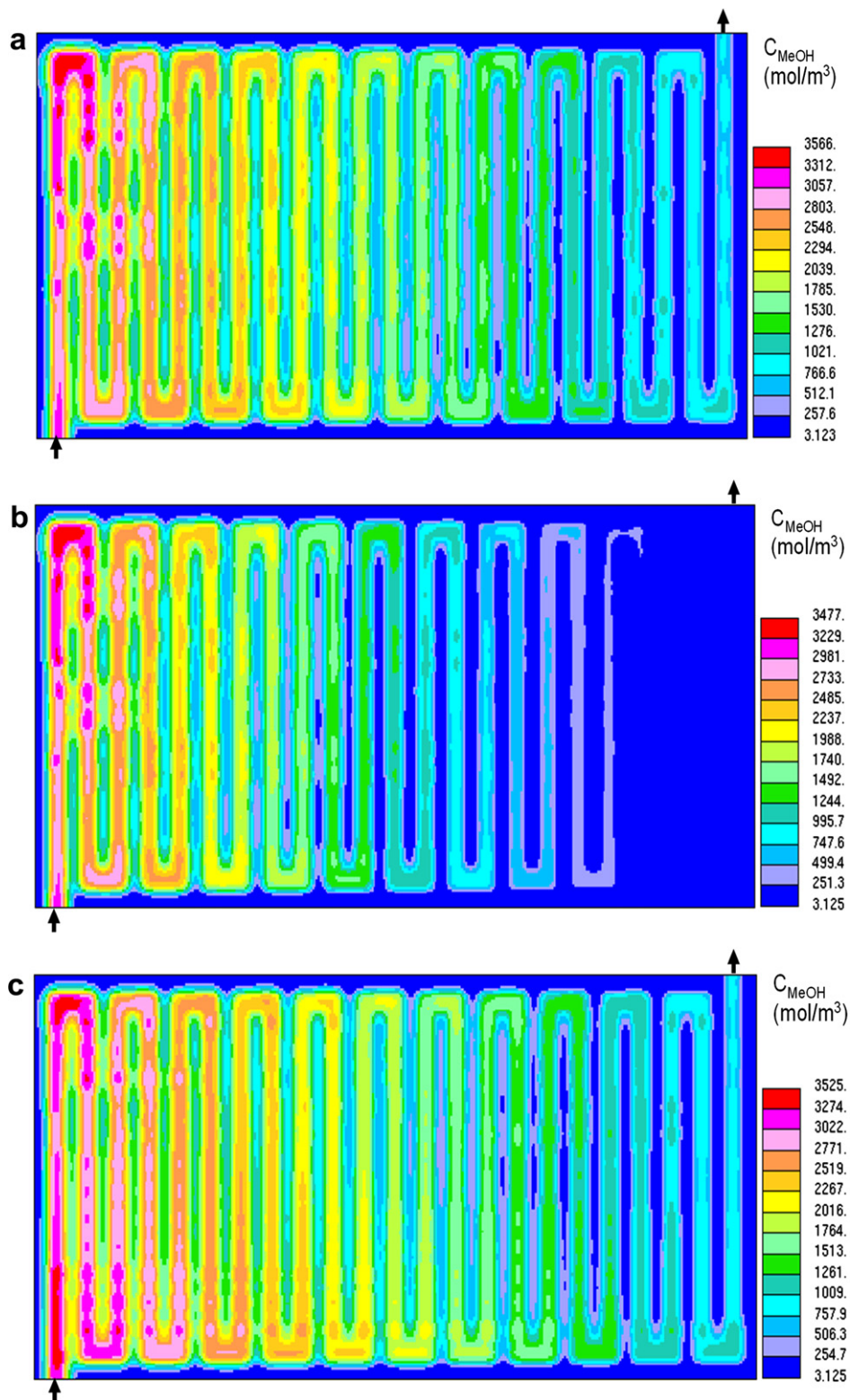


Fig. 16. Methanol concentration (mol m^{-3}) in the anode catalyst layer of the full-scale cell (28 cm^2) when $T_{\text{cell}} = 313 \text{ K}$, $RH = 10\%$, $C_{\text{MeOH}} = 4 \text{ M}$, and $I = 150 \text{ mA cm}^{-2}$: (a) $\xi_a = 2.0$ and $\zeta_c = 2.0$ (case A), (b) $\xi_a = 1.4$ and $\zeta_c = 2.0$ (case B), (c) $\xi_a = 2.0$ and $\zeta_c = 5.0$ (case C).

implies that the outlet region may suffer from methanol shortage problem. As the crossover current density is a strong function of the methanol concentration, the crossover current density shown in Fig. 17 has similar distribution trend with Fig. 16.

3.2.2. Current density distribution

As shown in the single channel model, current density distribution becomes more uniform when the stoichiometry increases (see Fig. 18). For the same anode/cathode stoichiometry condition with counter-flow configuration, the highest current density is

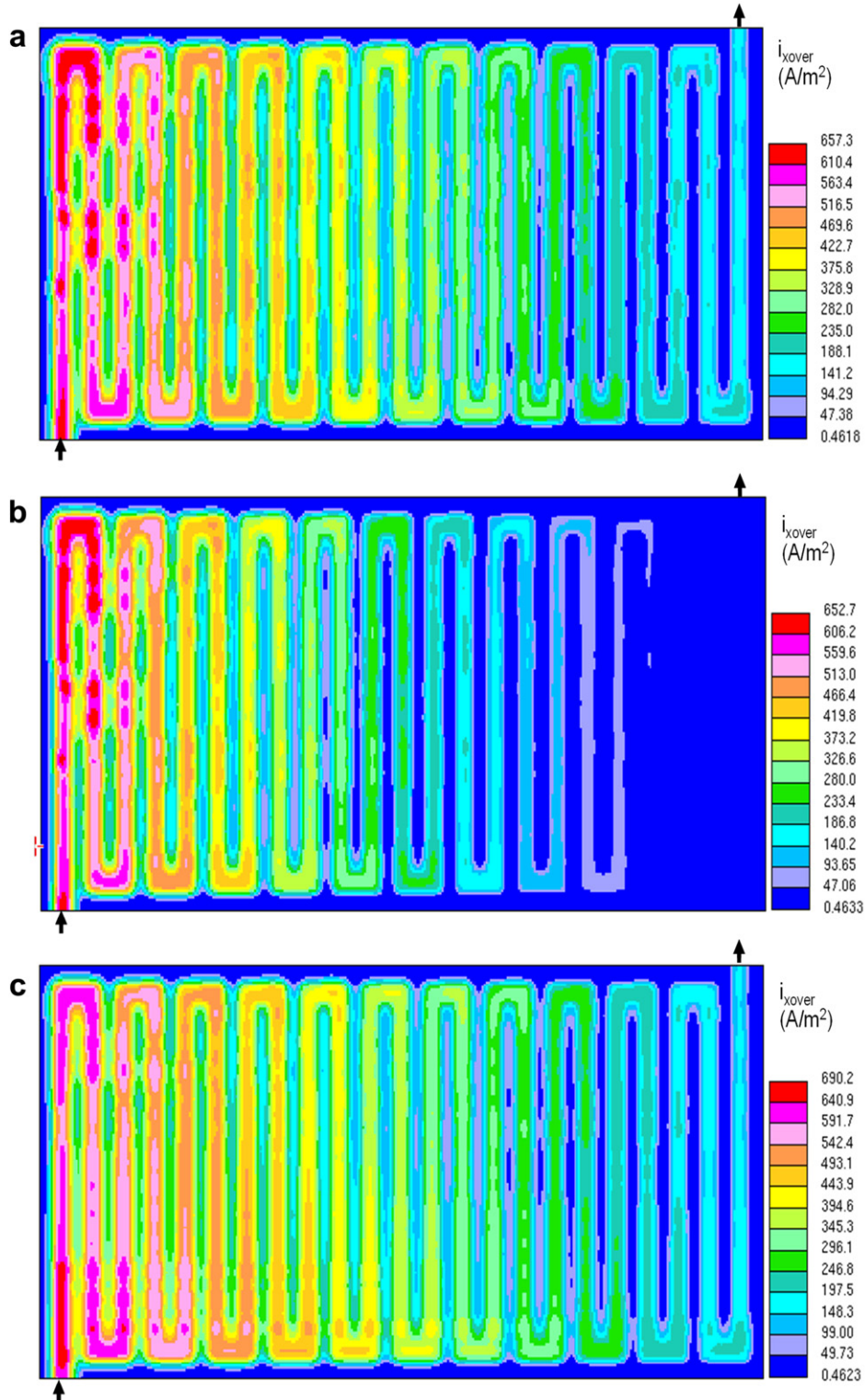


Fig. 17. Crossover current density ($A\ m^{-2}$) distribution of the full-scale cell ($28\ cm^2$) when $T_{cell} = 313\ K$, $RH = 10\%$, $C_{MeOH} = 4\ M$, and $I = 150\ mA\ cm^{-2}$: (a) $\zeta_a = 2.0$ and $\zeta_c = 2.0$ (case A), (b) $\zeta_a = 1.4$ and $\zeta_c = 2.0$ (case B), (c) $\zeta_a = 2.0$ and $\zeta_c = 5.0$ (case C).

found on the cathode side (low half region in case A). This is because ORR is more active than MOR and the anode inlet side suffers from methanol crossover which degrades the cell performance.

Note cathode inlet port (B in Fig. 18(a)) and outlet port region (A in Fig. 18(a)) show relatively lower current density than other region in when anode stoichiometry is large enough (case A and C). Firstly, those regions are corners of the anode channel where

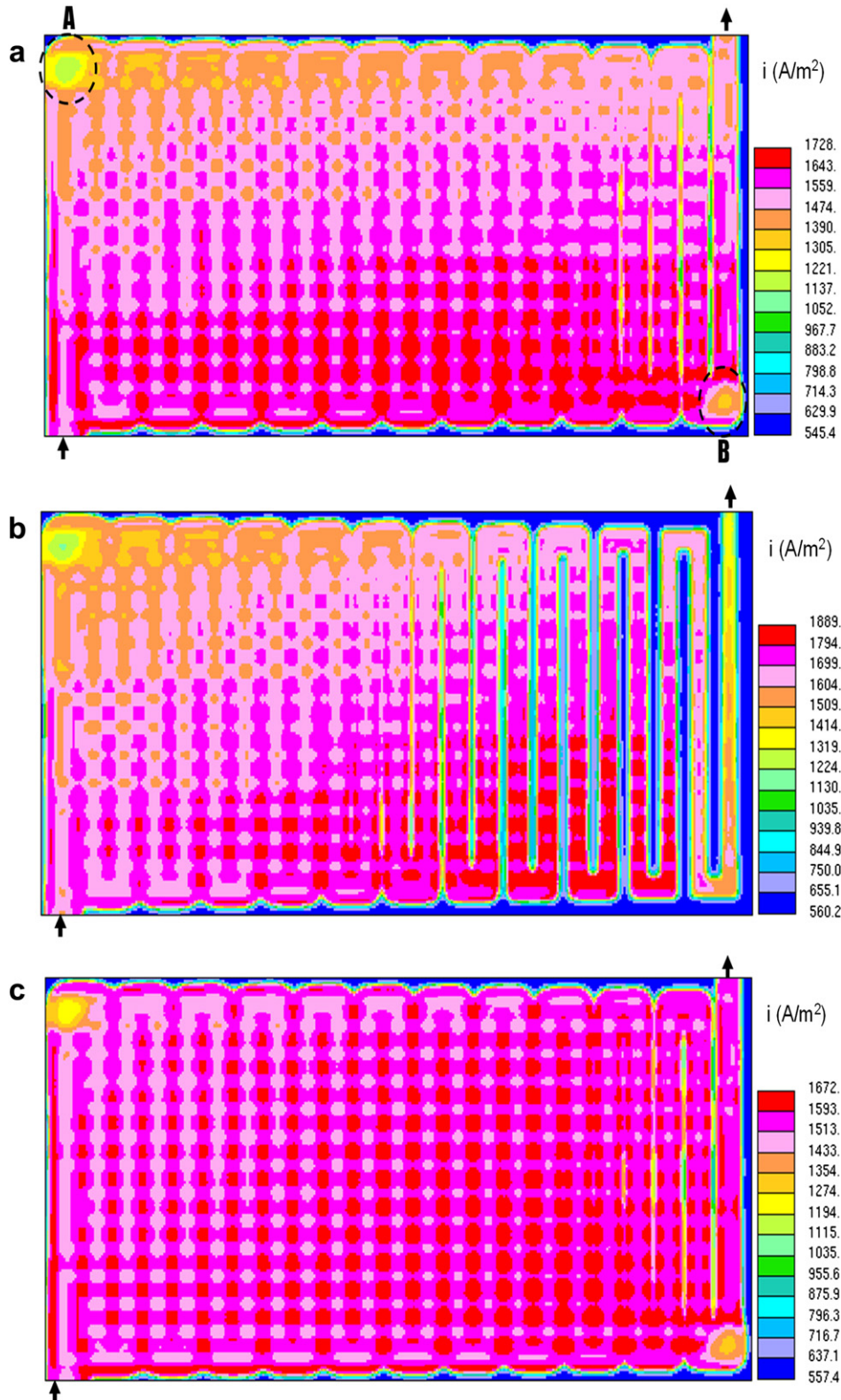


Fig. 18. Current density (A m^{-2}) distribution in the membrane of the full-scale cell (28 cm^2) when $T_{\text{cell}} = 313 \text{ K}$, $RH = 10\%$, $C_{\text{MeOH}} = 4 \text{ M}$, and $I = 150 \text{ mA cm}^{-2}$: (a) $\zeta_a = 2.0$ and $\zeta_c = 2.0$ (case A), (b) $\zeta_a = 1.4$ and $\zeta_c = 2.0$ (case B), (c) $\zeta_a = 2.0$ and $\zeta_c = 5.0$ (case C).

fuel concentration is greater than neighboring region due to the improved mixing effect (see Fig. 16). Secondly, those regions have the widest cathode channel area (three times large area than a single channel area) since two cathode channels merges together there, which means oxygen is widely spread there. Therefore, large amount of methanol crossovered to the cathode

side reacts very actively with oxygen there, which degrades the cell performance.

3.2.3. Temperature distribution

As the cathode catalyst generates more heat than the anode catalyst, temperature distribution follows the cathode channel

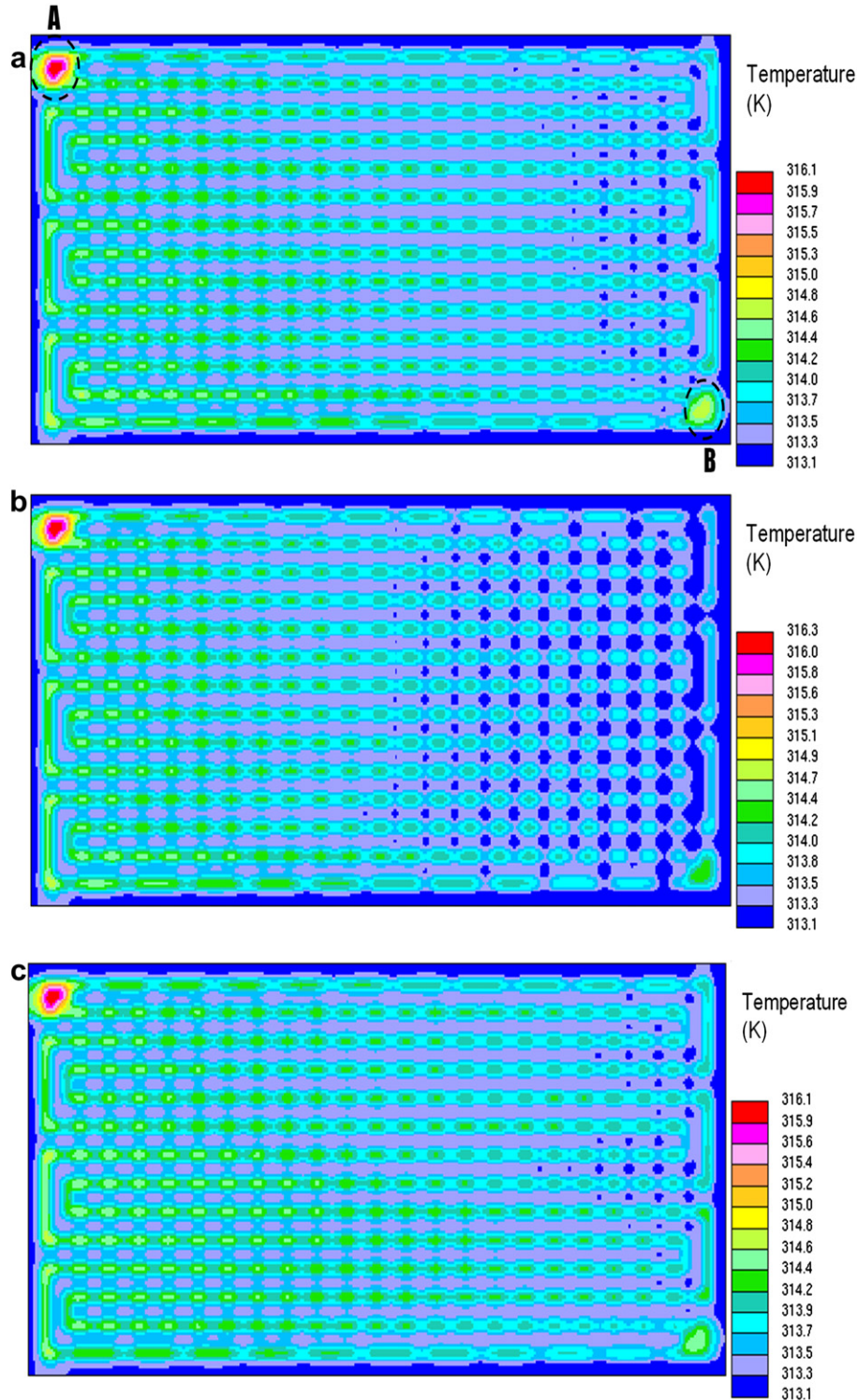


Fig. 19. Temperature (K) distribution in the membrane of the full-scale cell (28 cm^2) when $T_{\text{cell}} = 313 \text{ K}$, $RH = 10\%$, $C_{\text{MeOH}} = 4 \text{ M}$, and $I = 150 \text{ mA cm}^{-2}$: (a) $\zeta_a = 2.0$ and $\zeta_c = 2.0$ (case A), (b) $\zeta_a = 1.4$ and $\zeta_c = 2.0$ (case B), (c) $\zeta_a = 2.0$ and $\zeta_c = 5.0$ (case C).

shape as shown in Fig. 19. Left half region is hotter than right half region since methanol crossover concentrated in the left half region generates additional heat. Again, hot spots are found in region A and B where methanol crossover is strong and cathode area is wide.

3.2.4. Effect of stoichiometry

Comparing case A and case B, it is observed that increasing fuel stoichiometry improves cell voltage while worsening fuel efficiency (large methanol crossover). Comparing case A and case C, it is noticeable that increasing air stoichiometry worsens fuel efficiency also although cell voltage improves. This is because improved oxygen reduction reaction in the cathode catalyst layer due to large air stoichiometry induces more methanol crossover through the membrane.

4. Conclusion

Through the developed non-isothermal multi-dimensional DMFC model which is capable of simulating saturation jump at the interface of different porous media, the effectiveness of the both anode and cathode MPL is confirmed. Non-isothermal behavior including thermal diffusion and phase change is examined and it is found that heat and water management are strongly coupled with each other by the material property (heat conductivity) and the cell operating condition (temperature and inlet air humidity). Finally, local distribution of current and methanol concentration are examined with a full-scale simulation of 28 cm² DMFC cell.

List of symbols

<i>A</i>	area (m ²)
<i>a</i>	specific reaction area (m ² m ⁻³)
<i>ABP (abp)</i>	anode bipolar plate
<i>ACL (acl)</i>	anode catalyst layer
<i>ADL (adl)</i>	anode gas diffusion layer
<i>AML (aml)</i>	anode micro-porous layer
<i>c_p</i>	specific heat (J kg ⁻¹ K)
<i>c</i>	concentration (mol m ⁻³)
<i>CBP (cbp)</i>	cathode bipolar plate
<i>CCL (ccl)</i>	cathode catalyst layer
<i>CDL (cdl)</i>	cathode gas diffusion layer
<i>CML (cml)</i>	cathode micro-porous layer
<i>d</i>	Thickness (m)
<i>D</i>	diffusivity (m ² s ⁻¹)
<i>F</i>	Faraday constant (C mol ⁻¹)
<i>GDL</i>	gas diffusion layer
<i>h</i>	heat transfer coefficient (W m ⁻² K), mass transfer coefficient (m s ⁻¹)
<i>I</i>	current (A)
<i>i</i>	current density (Am ⁻²)
<i>j</i>	phase-diffusion flux (mol m ⁻² s), volumetric current density (A m ⁻³)
<i>J</i>	Leverette function
<i>k</i>	thermal conductivity (W m ⁻¹ K)
<i>k_H</i>	Henry's constant
<i>k_r</i>	relative permeability
<i>K_c</i>	rate constant
<i>K</i>	permeability (m ²)
<i>m</i>	mass (kg)
<i>M</i>	molar weight
<i>MEM (mem)</i>	membrane
<i>MCO</i>	methanol crossover rate

<i>MPL (mpl)</i>	micro-porous layer
<i>N</i>	molar flux (mol m ⁻² s)
<i>p</i>	pressure (Pa)
<i>R</i>	gas constant (J K ⁻¹ mol)
<i>RH</i>	relative humidity (%)
<i>s</i>	liquid saturation, entropy
<i>S</i>	source term (mol m ⁻³ s), (W m ⁻³)
<i>T</i>	temperature (K)
<i>u</i>	velocity (m s ⁻¹)
<i>V</i>	volume (m ³)
<i>Y</i>	species mass fraction

Greek

<i>α</i>	transfer coefficient, net water transfer coefficient
<i>δ</i>	Thickness (m)
<i>ε</i>	porosity
<i>Φ</i>	phase potential (V)
<i>η</i>	overpotential (V)
<i>κ</i>	ionic conductivity (S m ⁻¹)
<i>λ</i>	relative mobility, water content
<i>μ</i>	viscosity (kg m ⁻¹ s)
<i>ν</i>	kinetic viscosity (m ² s ⁻¹)
<i>θ</i>	angle (°)
<i>ρ</i>	density (kg m ⁻³)
<i>σ</i>	Surface tension (N m ⁻¹)
<i>ξ</i>	stoichiometry
<i>τ</i>	shear stress (Pa)
<i>Ω</i>	ohmic

Superscripts and subscripts

<i>A</i>	anode
<i>b</i>	breakthrough
<i>c</i>	cathode, contact
<i>capill</i>	capillary
<i>d</i>	drag
<i>diff</i>	diffusion
<i>e</i>	electrolyte phase
<i>eff</i>	effective
<i>g</i>	gas
<i>hp</i>	hydraulic permeation
<i>i</i>	species
<i>k</i>	species
<i>l</i>	liquid
<i>m</i>	mass
<i>mem</i>	membrane, methanol
<i>0</i>	reference
<i>ref</i>	reference
<i>s</i>	solid phase
<i>sat</i>	saturated
<i>tot</i>	total
<i>T</i>	temperature
<i>xover</i>	crossover

References

- [1] A. Blum, T. Duvdevani, M. Philosoph, N. Rudoy, E. Peled, J. Power Sources 117 (2003) 22.
- [2] Z.H. Wang, C.Y. Wang, J. Electrochem. Soc. 150 (2003) A508.
- [3] W. Liu, C.Y. Wang, J. Electrochem. Soc. 154 (2007) B352.
- [4] J.H. Nam, M. Kaviany, Int. J. Heat Mass Transfer 46 (2003) 4595.
- [5] U. Pasaogullari, C.Y. Wang, Electrochem. Acta 49 (2004) 4359.
- [6] C.Y. Wang, P. Cheng, Int. J. Heat Mass Transfer 39 (1996) 3607.
- [7] J.P. Meyers, J. Newman, J. Electrochem. Soc. 149 (2002) A710.
- [8] J.P. Meyers, J. Newman, J. Electrochem. Soc. 149 (2002) A718.
- [9] J.P. Meyers, J. Newman, J. Electrochem. Soc. 149 (2002) A729.
- [10] W. Liu, C.Y. Wang, J. Power Sources 164 (2007) 189.

- [11] Z. Qi, A. Kaufman, J. Power Sources 109 (2002) 38.
- [12] C.E. Shaffer, C.Y. Wang, Electrochim. Acta 54 (2009) 5761.
- [13] F. Liu, C.Y. Wang, Electrochim. Acta 53 (2008) 5517.
- [14] S. Basu, C.Y. Wang, K.S. Chen, J. Electrochem. Soc. 156 (2009) B748.
- [15] R.H. Brooks, A.T. Corey, Hydrology Papers, vol. 3, Colorado State University, 1964, 1.
- [16] R.B. Mrazek, C.E. Wicks, K.N.S. Prabhu, J. Chem. Eng. Data 13 (1968) 508.
- [17] B.E. Poling, J.M. Prausnitz, J.P. O'Connell, The Properties of Gases and Liquids, fifth ed., McGraw-Hill, New York, 2001.
- [18] Z.J. Derlacki, A.J. Easteal, V.J. Edge, L.A. Woolf, Z. Roksandic, J. Phys. Chem. 89 (1985) 5318.
- [19] T.E. Springer, T.A. Zawodzinski, S. Gottesfeld, J. Electrochem. Soc. 138 (1991) 2334.
- [20] T.A. Zawodzinski, C. Derouin, S. Radzinski, R.J. Sherman, V.T. Smith, T.E. Springer, S. Gottesfeld, J. Electrochem. Soc. 140 (1993) 1041.
- [21] G. Lu, C.Y. Wang, An Invited Chapter for New Developments in Heat Transfer (2005). 317 (Chapter 9).
- [22] T.A. Zawodzinski, J. Davey, J. Valerio, S. Gottesfeld, Electrochim. Acta 40 (1995) 297.